The Astrophysical Journal, 1008:67 (26pp), 2026 September 1 https://doi.org/10.3847/1538-4357/ae88e9
© 2026. The Author(s). Published by the American Astronomical Society.
OPEN ACCESS

Benchmark Brown Dwarf Systems. I. Chemical Abundance Analysis of FGK Stars with Wide-separation Brown Dwarf Companions Using PEPSI

Caprice L. Phillips[1,16], Megan Bedell[2], Catherine Manea[3], Alison Duck[4], Anusha Pai Asnodkar[5], Emily J. Griffith[6,17], Austin Rothermich[7,8,9], Emily Calamari[10], Jacqueline K. Faherty[10], Ben Burningham[11], Channon Visscher[12,13], Eileen C. Gonzales[14], Ilya Ilyin[15], Klaus Strassmeier[15], and Ji Wang[4]
[1] Department of Astronomy & Astrophysics, University of California, Santa Cruz, CA 95064, USA; cphillips@ucsc.edu
[2] Center for Computational Astrophysics, Flatiron Institute, 162 Fifth Avenue, New York, NY 10010, USA
[3] Department of Physics & Astronomy, University of Utah, Salt Lake City, UT 84112, USA
[4] Department of Astronomy, The Ohio State University, 100 W. 18th Avenue, Columbus, OH 43210, USA
[5] Department of Astronomy, California Institute of Technology, Pasadena, CA 91125, USA
[6] Center for Astrophysics and Space Astronomy, Department of Astrophysical and Planetary Sciences, University of Colorado, 389 UCB, Boulder, CO 80309-0389, USA
[7] Department of Astrophysics, American Museum of Natural History, Central Park West at 79th Street, NY 10024, USA
[8] Department of Physics, Graduate Center, City University of New York, 365 5th Avenue, New York, NY 10016, USA
[9] Department of Physics and Astronomy, Hunter College, City University of New York, 695 Park Avenue, New York, NY 10065, USA
[10] Department of Astrophysics, American Museum of Natural History, New York, NY 10024, USA
[11] Centre for Astrophysics Research, School of Physics, Astronomy and Mathematics, University of Hertfordshire, Hatfield AL10 9AB, UK
[12] Chemistry & Planetary Sciences, Dordt University, Sioux Center, IA 51250, USA
[13] Center for Exoplanetary Systems, Space Science Institute, Boulder, CO 80301, USA
[14] Department of Physics & Astronomy, San Francisco State University, San Francisco, CA 94132, USA
[15] Leibniz-Institute for Astrophysics Potsdam (AIP), An der Sternwarte 16, D-14482 Potsdam, Germany
Received 2026 April 2; revised 2026 July 8; accepted 2026 July 8; published 2026 August 26

Abstract

We present results from a spectroscopic survey of 32 FGK stars hosting brown dwarfs, using high-resolution optical spectra (R = 130,000 and 50,000) obtained with the Potsdam Echelle Polarimetric and Spectroscopic Instrument spectrograph on the Large Binocular Telescope. The primary goal of this survey is to determine precise stellar parameters and abundances for 11 elements (C, O, Mg, Si, Ca, Al, Ti, Fe, Y, S, and N) in these systems. We employ spectral synthesis within the BACCHUS framework to derive precise stellar properties and elemental abundance ratios. For our data with average signal-to-noise ratio > 200, we achieve a typical error of 42 K in $T_{\rm eff}$ and ∼0.03 dex for [Fe/H]. We observe a significant dispersion from a solar C/O ratio among the sample of brown dwarf host stars that host primarily wide-orbit brown dwarfs. Using established theoretical chemical frameworks, we discuss the implications of the observed Mg/Si and Ca/Al ratios for cloud properties in the brown dwarf companions. Finally, we evaluate the applicability of the [Y/Mg] stellar clock for our sample and discuss the broader implications of our results. This work provides a timely and uniform abundance analysis of host stars, supporting extended wavelength brown dwarf observations in the era of JWST.

Unified Astronomy Thesaurus concepts: Stellar abundances (1577); F stars (519); Brown dwarfs (185); G stars (558); K stars (878); High resolution spectroscopy (2096)

1. Introduction

Brown dwarfs are a category of astronomical objects with initial mass (⩽0.072 $M_{\odot}$) insufficient to maintain stable hydrogen fusion. As a result, these objects invariably contract and cool throughout their lifetimes (G. Chabrier & I. Baraffe 1997) and progress through their spectral classification sequence (M, L, T, and Y) (J. D. Kirkpatrick 2005). This cooling provides a challenge in understanding formation history and evolution, as it results in a mass−temperature −age degeneracy (J. I. Canty et al. 2013; J. R. Crepp et al. 2016). One path forward to break this degeneracy is through the study of benchmark systems. Benchmark brown dwarfs can include systems in which properties such as mass, age, and chemistry may be determined independently and precisely (K. M. Aller et al. 2016; G. M. Brandt et al. 2021; C. L. Phillips et al. 2024; E. L. Rickman et al. 2024; A. Rothermich et al. 2024; Z. H. Zhang et al. 2025). Age-benchmarked brown dwarfs include those that are members of young moving groups, associations, or stellar clusters, where the coeval members have known ages from age-dating mechanisms that can include isochrone fitting, kinematic traceback, and chromospheric activity or X-ray emission (V. G. Ortega et al. 2007; J. Gagné 2024; J. Lee & I. Song 2024). Dynamical mass provides the most direct and model-independent measurement of the mass of brown dwarfs (T. J. Dupuy et al. 2014; G. M. Brandt et al. 2021; K. Franson & B. P. Bowler 2023). As a result, accurate dynamical masses enable stringent tests of substellar evolutionary and atmospheric models, which can improve our understanding of brown dwarf formation and evolution (K. Franson et al. 2022; A.-L. Maire et al. 2024).

In recent works, E. Calamari et al. (2024) focused on compositional benchmarks, defined as "benchmark brown dwarfs belonging to a binary or multiple system with the

[16] NASA Sagan Fellow.
[17] NASA Hubble Fellow.

Original content from this work may be used under the terms of the Creative Commons Attribution 4.0 licence. Any further distribution of this work must maintain attribution to the author(s) and the title of the work, journal citation and DOI.

specification that the primary star in the system is of spectral type F, G, or K." By studying a sample of solar-type (FGK) stars hosting a brown dwarf companion, we can place system constraints on atomic and molecular abundances in order to inform our subsequent companion studies. E. Calamari et al. (2024) established the underlying theoretical framework and derived the chemical relationships linking stellar and substellar compositions, providing a foundation for interpreting benchmark systems. FGK-type stars are ideal candidates for detailed compositional analysis, allowing for more accurate determination of elemental abundances, such as carbon, nitrogen, oxygen, magnesium, silicon, and other heavy elements, which will be valuable for future studies. Although such benchmark systems provide valuable constraints on brown dwarf compositions, they represent a relatively small and specialized subset of the overall brown dwarf population, as most brown dwarfs are typically found in isolation (J. K. Faherty et al. 2016; C. Fontanive et al. 2023). Compositional benchmarks can include close companions and widely separated companions to well-characterized stars. In this work, we focus on wide-companion systems, with projected separations >100 au. Brown dwarf companions at wide separations are rare, with the frequency of wide-orbit systems estimated to be ~1.3% (N. Grieves et al. 2017; F. Kiefer et al. 2019; F. Feng et al. 2022). Similarly, the detection frequency of brown dwarfs around solar-like stars is low, at 2.0% ± 0.5% (F. Kiefer et al. 2019). Given their rarity yet valuable power, it is essential to extract as much information as possible from these systems, including atmospheric composition, temperature, surface gravity, and cloud properties, while also leveraging the host star abundances as a reference point for interpreting substellar compositions.

Stellar abundances are a quintessential component of our understanding of the planet and brown dwarf formation process and mechanisms (J. K. Teske 2024, and references therein). While stellar compositions cannot be mapped directly into the bulk chemistry of planets, they establish the initial chemical reservoir from which planets form. In the substellar (brown dwarf) regime, stellar abundances more directly trace the formation environment of brown dwarfs, offering key constraints on their origins. In this work, we assume that brown dwarf companions retain the bulk elemental abundance patterns of their host stars, an assumption we revisit in Section 5.2.1. In many studies of brown dwarf and exoplanet atmospheres, host star abundances are often assumed to be solar for simplicity; however, this assumption can introduce significant biases in the interpretation of atmospheric retrievals and forward models (J. W. Xuan et al. 2024a; P. Baghel et al. 2025; W. W. Meynardie et al. 2025; A. Baburaj et al. 2026). This is particularly evident in the directly imaged planets and planetary-mass companions such as β Pictoris b and Ross 458C, where inferred formation interpretations are sensitive to the assumed composition of the host stars (R. Landman et al. 2024; H. Reggiani et al. 2024; W. W. Meynardie et al. 2025). Stellar compositions can vary substantially across the Galactic population (N. Cabral et al. 2023; J. Teixeira et al. 2025), with differences in metallicity and elemental ratios (e.g., C/O, Mg/Si, [Fe/H]), directly influencing the chemistry and cloud formation of their substellar companions, as explored in E. Calamari et al. (2024). A well-characterized host star thus serves as a compositional anchor by enabling a more precise linkage between stellar and substellar chemistry, reducing degeneracies in retrieval analyses, and ensuring that interpretation of formation pathways is physically meaningful (J. R. Kolecki & J. Wang 2022; A. S. Polanski et al. 2022; R. da Silva et al. 2024; Q. Sun et al. 2025).

We present uniform abundance measurements for 11 elements for 32 stars with known brown dwarf companions. We provide diagnostic uses of the C/O, Mg/Si, Ca/Al, [Y/Mg], and S/N ratios for useful information regarding formation, age, and metallicity for this critical sample. In Section 2, we describe the observing campaign for our data. In Section 3, we describe our methodology and analysis technique using the BACCHUS framework. In Section 4 we validate our results with the Sun and comparison to literature values. We provide discussions and implications for our work in Sections 5 and 6, respectively, and we conclude in Section 7.

2. Data

2.1. Sample Selection

We collected 32 high-resolution spectra of FGK hosts of primarily wide-orbit brown dwarfs (>100 au)—with the exception of HD 89744 (63 au) and BD +01 299 (35−45 au). These wide-orbit brown dwarfs can be observed without the interference of light from their host stars, which affects close-in orbits. The host stars for the companion systems are known nearby stars, and some of our targets have been previously observed as part of exoplanet and stellar observing campaigns (e.g., SPFOT, Luck, and SONS surveys; W. S. Holland et al. 2017; R. E. Luck 2018; E. Stonkutė et al. 2020). Abundances for these stars have not necessarily been investigated or reported in a uniform catalog or dataset. We highlight the importance of a uniform analysis for our sample, as N. R. Hinkel et al. (2016) found that choice of datasets, methodology, and analysis can lead to discrepancies between stellar parameters and abundances. We first compile our stellar sample from a previous literature collection of compositional benchmark brown dwarfs from E. Calamari et al. (2024). We prioritize stars that have brown dwarf targets observed as part of separate JWST programs: GO #3670 (PI: Burningham; B. Burningham et al. 2023) and GO #8140 (PI: Zhang; Z. Zhang et al. 2025a). Our sample also consists of newly discovered brown dwarf companions in the solar neighborhood, identified through the citizen science project, Backyard Worlds: Planet 9 (A. Rothermich et al. 2024). An overview of the systems selected for this study is presented in Tables 1 and 2.

2.2. Observations

We collect spectra from the Potsdam Echelle Polarimetric and Spectroscopic Instrument (PEPSI; K. G. Strassmeier et al. 2015) on the Large Binocular Telescope (LBT) between 2023 February 8 and 2024 January 16. PEPSI is a high-resolution echelle spectrograph with two arms (red and blue) that cover the wavelength range of 383–914 nm across six different cross dispersers (CDs). The primary CDs used in this work are CD III (4800−5441 Å) and CD VI (7419−9140 Å). These CDs were chosen because they house many key lines, including the O I triplet needed to calculate the [O/H] abundance and thus the C/O ratio. Most of our observations were taken with the 200 μm fiber yielding a 2-pixel sampled resolution of R = 130,000. In our initial observation campaign, five

Table 1
Observing Details

Object	V	Date	Exp (s)	$SNR_{CD\ II}$	$SNR_{CD\ III}$	$SNR_{CD\ VI}$	Resolution (R)
HD 89744	5.72	2023-11-03	15.0	⋯	249	285	130,000
HD 46588	5.41	2023-02-08	50.0	⋯	657	889	50,000
*54 Psc	5.87	2023-11-02	34.0	⋯	406	532	130,000
V* HN Peg	5.95	2021-10-22	50.0	⋯	375	298	130,000
HD 126053	6.24	2023-02-08	70.0	⋯	467	664	50,000
GJ 417	6.40	2023-02-08	120.0	⋯	887	1149	50,000
HIP 9269	7.14	2023-10-22	170.0	⋯	533	519	130,000
G171-58	7.55	2024-01-16	150.0	⋯	370	361	130,000
HIP 26653	7.82	2023-11-04	180.0	⋯	370	459	130,000
HD 106888	8.15	2024-01-16	160.0	⋯	256	312	130,000
HD 51400	8.35	2023-11-04	170.0	⋯	225	380	130,000
HD 203030	8.43	2023-10-22	513.0	⋯	461	481	130,000
HD 8291	8.60	2023-11-06	180.0	⋯	239	272	130,000
HD 16270	8.32	2023-11-06	210.0	⋯	243	291	130,000
HD 116012	8.59	2023-02-08	660.0	⋯	763	1124	50,000
BD +21 55	9.19	2023-10-22	1113.0	⋯	514	601	130,000
BD +60 1417	9.43	2023-02-08	1260.0	⋯	517	795	50,000
StKM 2-1777	9.29	2023-10-22	1500.0	⋯	560	869	130,000
HD 253662	9.91	2023-11-02	600.0	⋯	265	297	130,000
CD –24 407	9.94	2023-09-15	2000.0	⋯	⋯	⋯	130,000
BD +13 2269	10.36	2024-01-14	3420.0	⋯	234	311	130,000
BD +01 299	10.16	2023-11-06	1200.0	⋯	316	474	130,000
StKM 1-1526	10.41	2023-09-15	4140.0	⋯	⋯	⋯	130,000
TYC 5213-545-1	10.94	2023-09-15	4920.0	⋯	⋯	⋯	130,000
LP 617-58	11.23	2024-01-16	1919.0	⋯	91	148	130,000
HIP 63506	11.24	2024-01-14	4007.0	⋯	175	329	130,000
LSPM J0632+5053	9.97	2023-11-02	590.0	⋯	237	288	130,000
NLTT 1011	10.89	2023-11-02	1792.0	⋯	240	374	130,000
HD 125141 (G200 -28)	7.63	2023-02-08	90.0	⋯	230	611	130,000
BD +06 2986	9.77	2023-05-01	5000.0	186	⋯	817	130,000
BD +24 4329	9.81	2023-06-19	3800.0	217	⋯	680	130,000
BD +49 2561	10.09	2023-05-01	5000	218	⋯	650[a]	130,000

Notes. V magnitude, observing date, exposure time, and SNR per pixel in all objects.
[a] We use observations from 2023-05-01 for this target for CD VI.

systems (HD 46588, HD 126054, GJ 417, HD 116012, BD +60 1417) were observed with the 300 μm fiber, resulting in a resolution of $R = 50{,}000$ instead of $R = 130{,}000$. We discuss how this difference in resolution affects our results in Section 3.3. Full observation details are provided in Table 1.

We employ the spectroscopic data systems for PEPSI pipeline (SDS4PEPSI) to reduce the spectra of our targets, as described in K. G. Strassmeier et al. (2018b). In short, this pipeline applies bias and flat-field corrections and estimates the photon-noise contribution to the spectra. It removes contamination from scattered light and cosmic rays. The pipeline conducts flux extraction, and wavelength calibrates the spectra against Th-Ar lines, as well as corrects for the echelle's blaze function, fringing, and vignetting effects. Finally, the pipeline corrects for the star's radial velocity shifts to bring the spectra to rest-frame wavelengths and applies a continuum normalization by fitting a 2D smoothing spline in the cross-dispersion and dispersion directions. While the pipeline's default continuum normalization removes much of the continuum variation, we found that our abundance measurements were sensitive to small continuum deviations that were not fully corrected by the pipeline. To fix this, we perform a second step of continuum normalization with a low-order polynomial fit individually to each of the two dispersers. Specifically, we perform iterative one-sided sigma-clipping to select continuum pixels in each wavelength region and then fit a third-order polynomial (for CD III) or a fifth-order polynomial (for CD VI) to these continuum pixels and divide the data by the best-fit polynomial to continuum normalize. A portion of the normalized spectra for our sample are shown in Figure 1.

3. Methods

3.1. Photometric Stellar Parameters

The photometric stellar properties were estimated from spectral energy distributions (SEDs) with `EXOFASTv2` (J. Eastman et al. 2012, 2019). These photometric stellar properties were then used as starting values for our analysis of stellar properties from the PEPSI spectra. `EXOFASTv2` is based on a differential evolution Markov Chain Monte Carlo (MCMC) method to simultaneously characterize exoplanets and their host stars. Here we use the MIST isochrones (A. Dotter 2016) fit jointly with an SED to characterize our host stars. We place no prior on the metallicity or temperature of these stars. We use broadband photometry measurements from Gaia DR3 RGB magnitudes (Gaia Collaboration et al. 2023), Two Micron All Sky Survey (2MASS) JHK_s magnitudes (R. M. Cutri et al. 2003), and Wide-field Infrared Survey Explorer (WISE) 1, 2, 3, and 4 mag (E. L. Wright et al. 2010) to construct the SED

Table 2
Host Star Information and Companion Information Organized by Host Spectral Type

Star Name	SpT Primary	Companion	SpT Secondary	$d_{\rm HostStar}$ (pc)	Proj. Sep (au)	References
HD 89744	F7	HD 89744 B[a]	L0.5	38.68 ± 0.11	63	(1), (5)
HD 46588	F7V	HD 46588 B[a]	L9	18.21 ± 0.04	1420	(1), (6)
G171-58 (HD 2057)	F8	2MASS J00250365+4759191	L4+L4	54.01 ± 0.40	8800	(7)
HD 106888	F8	2MASS J12173646+1427119	L1	67.18 ± 0.57	2170	(1), (8)
V* HN Peg	G0V+	HN Peg B[a]	T2.5	18.13 ± 0.02	795	(1), (10)
HD 126053 (BD +01 2920)	G1.5V	BD +01 2920B	T8	17.44 ± 0.01	2630	(1), (2)
GJ 417	G2	GJ 417 BC[b]	L4.5+L6	22.65 ± 0.02	2000	(1), (10)
LSPM J0632+5053	G2V	2MASS J06324849+5053351[a]	L1.5	82.58 ± 0.13	4499	(11)
HD 51400	G5	CWISE J065752.45+163350.2	L6β	37.08 ± 0.78	2300	(1), (3)
HD 8291	G5V	HD 8291 B	L1+T3	50.38 ± 0.35	2570	(1), (11)
HD 125141 (G200-28)	G5	2MASS J14165987+5006258[a]	L4.5	47.11 ± 0.06	26951	(1), (12)
HIP 26653 (HD 37216)	G5V	HD 37216 B[a]	L5	28.08 ± 0.04	753	(1), (11)
HD 253662	G8IV	2MASS J06135342+1514062[b]	L0.5	86.46 ± 0.34	>1252	(1), (11)
LP 617-58	G8	CWISE J132539.70+022309.4	M9	118 ± 0.40	3600	(3)
HIP 9269 (HD 12051)	G9V	HIP 9269B[a]	L6	24.77 ± 0.02	1300	(1), (11)
*54 Psc (HD 3651)	K0.5V	HD 3651 B	T7.5	11.14 ± 0.01	480	(1), (11), (9)
HD 203030	K0V	HD 202030 B[b]	L7.5	39.29 ± 0.09	487	(1), (11)
HD 116012	K0V	2MASS J13204427+0409045	L5	30.31 ± 0.046	9708	(1), (13)
BD +60 1417	K0	WISE J124332.17+600126.6[b]	L8γ	44.96 ± 0.03	1662	(1), (14), (15)
TYC 5213-545-1	K0	CWISE J214129.80–024623.6	L4	78.99 ± 0.06	9000	(3)
BD +21 55	K2	2MASS J00302476+2244492	L0.5	55.21 ± 0.11	3970	(1), (11)
CD –24 407 (HIP 4417)	K2	CWISE J005635.48–240401.9	L8	67.60 ± 0.08	6924	(1), (3)
BD +49 2561	K2	CWISE J165325.10+490439.7	L5	57.06 ± 0.03	3000	(3)
BD +13 2269	K2	ULAS J103131.49+123736.4	L3	99.0 ± 0.20	4100	(3), (4)
HD 16270	K2.5Vk	HD 16270 B[a]	L1.5	21.22 ± 0.02	250	(1), (16)
StKM 1-1526	K4/5	CWISE J174509.03+380733.2	L4β	57.20 ± 0.03	3900	(3)
StKM 2-1777 (BD +29 5007)	K5V	WIS 395 B	L5.5	23.63 ± 0.02	22086	(1), (17)
HIP 63506 (BD +42 2363)	K6V	2MASS J13005061+4214473	L1	44.15 ± 0.06	5640	(1), (11)
BD +24 4329	K6V	CWISE J210640.16+250729.0[a]	T2	34.12 ± 0.02	38000	(3)
NLTT 1011 (LP 192-58)	K7	2MASS J00193275+4018576[a]	L2	55.21 ± 0.11	3990	(1), (11)
BD +01 299	K8V	ULAS J014016.91+015054.7	T5	38.56 ± 0.03	35–45	(4), (16)
BD +06 2986	K8V	ULAS J150457.65+053800.8	T6	19.02 ± 0.02	1230	(1), (11)

Notes.
[a] These targets were observed as a part of a JWST program with NIRSpec and MIRI instruments (GO #3670).
[b] These targets are observed and/or scheduled to be observed as a part of JWST programs with NIRSpec and/or MIRI instruments (GO #8140).
References. (1) Gaia Collaboration et al. (2023); (2) D. J. Pinfield et al. (2012); (3) A. Rothermich et al. (2024); (4) N. Skrzypek et al. (2016); (5) A. C. Schneider et al. (2014); (6) N. P. Loutrel et al. (2011); (7) I. N. Reid et al. (2006); (8) F. Marocco et al. (2017); (9) J. K. Faherty et al. (2009); (10) J. D. Kirkpatrick et al. (2000); (11) N. R. Deacon et al. (2014); (12) K. Chiu et al. (2006); (13) J. I. Gomes et al. (2013); (14) J. K. Faherty et al. (2021); (15) C. L. Phillips et al. (2024); (16) B. Burningham et al. (2018); (17) S. Baig et al. (2024).

in combination with the parallax from Gaia. By default, EXOFASTv2 requires a Gelman–Rubin score of 1.01 for models to be considered converged. Thus, the stellar evolution information from the MIST isochrones and the SED observations constrain estimates for stellar effective temperature and metallicity to be used as starting values for the analysis.

We note that the photometric stellar parameters used for initialization are not consistent with our derived spectroscopic parameters (Figure 2). Although the photometric values of $T_{\rm eff}$ and $\log g$ are obtained from observational data and serve as the basis for estimating physical properties such as stellar radius and mass, because we have magnitudes, SEDs, and parallaxes, their use prevents us from achieving ionization and excitation equilibrium between Fe I and Fe II abundances. Therefore, we adopt the spectroscopic parameters for subsequent abundance analyses, as they are optimized for this purpose. However, we emphasize that these spectroscopic parameters should alone not be used to infer the stellar mass or radius, as uncertainties in $\log(g)$ propagate into radius estimates, limiting the reliability of this approach (G. Torres et al. 2010; P. Jofré et al. 2019; A. Brucalassi et al. 2022).

3.2. Spectroscopic Parameters and Abundances

3.2.1. BACCHUS Code

We use the Brussels Automatic Code for Characterizing High accUracy Spectra (BACCHUS; T. Masseron et al. 2014) to derive spectroscopic parameters and elemental abundances for our sample. BACCHUS computes synthetic spectra for a range of abundances and compares these syntheses to observational data on a line-by-line basis, deriving abundances from different methods (e.g., using equivalent width, line depth, or χ^2). The synthetic spectra are calculated using the 1D LTE Turbospectrum radiative transfer code (R. Alvarez & B. Plez 1998; B. Plez 2012) and the MARCS model atmosphere grids (B. Gustafsson et al. 2008). BACCHUS uses four methods to compare the observed and synthetic spectra and provides an abundance measurement and associated

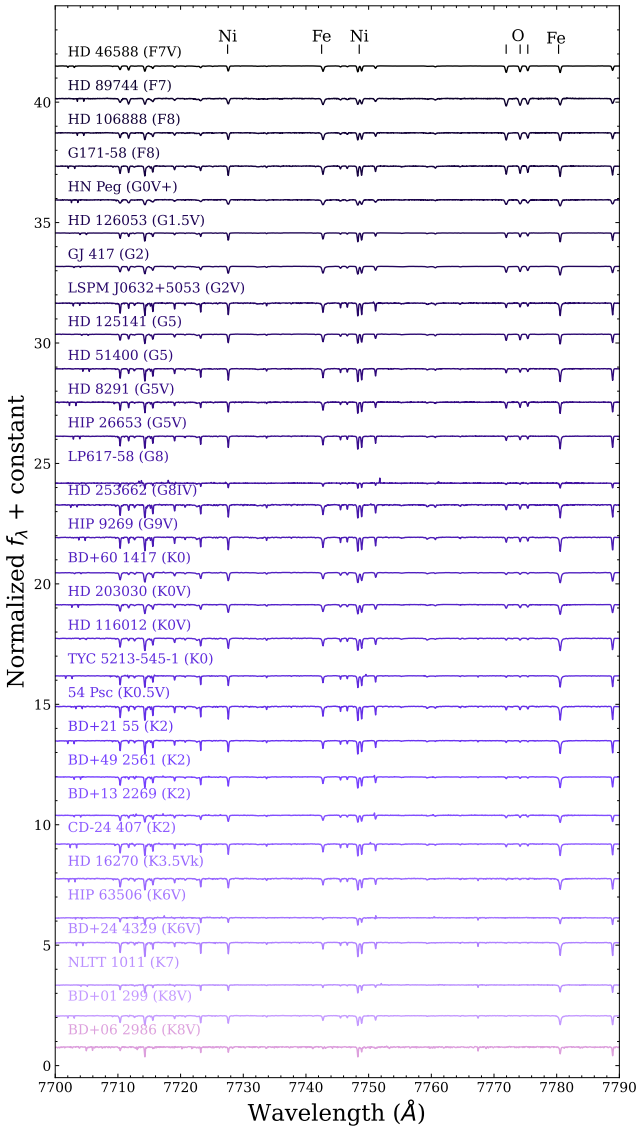


Figure 1. Subsets of our sample spectra in order of spectral class, from dark purple to light purple. Prominent absorption lines from oxygen triplet and iron (Fe) lines are labeled. Some nickel (Ni) lines are also labeled but are not used in this analysis.

quality flag for each method. The four methods are summarized as follows from C. R. Hayes et al. (2022):

1. A_{χ^2}: determines an abundance by minimizing the squared differences between synthetic and observed spectra.
2. $A_{\rm syn}$: looks for the abundance that makes the difference between the synthetic and the observed points zero.
3. $A_{\rm EW}$: determines the abundance needed to match the equivalent widths of the synthetic spectra to the observations.
4. $A_{\rm int}$: measures abundances by matching the line core in the synthetic and observed spectra.

We use the reduced PEPSI spectra to determine stellar parameters and abundances with BACCHUS. The fundamental stellar parameters are determined by BACCHUS using the excitation−ionization balance method. We start with our initial photometric estimates from EXOFASTv2, and

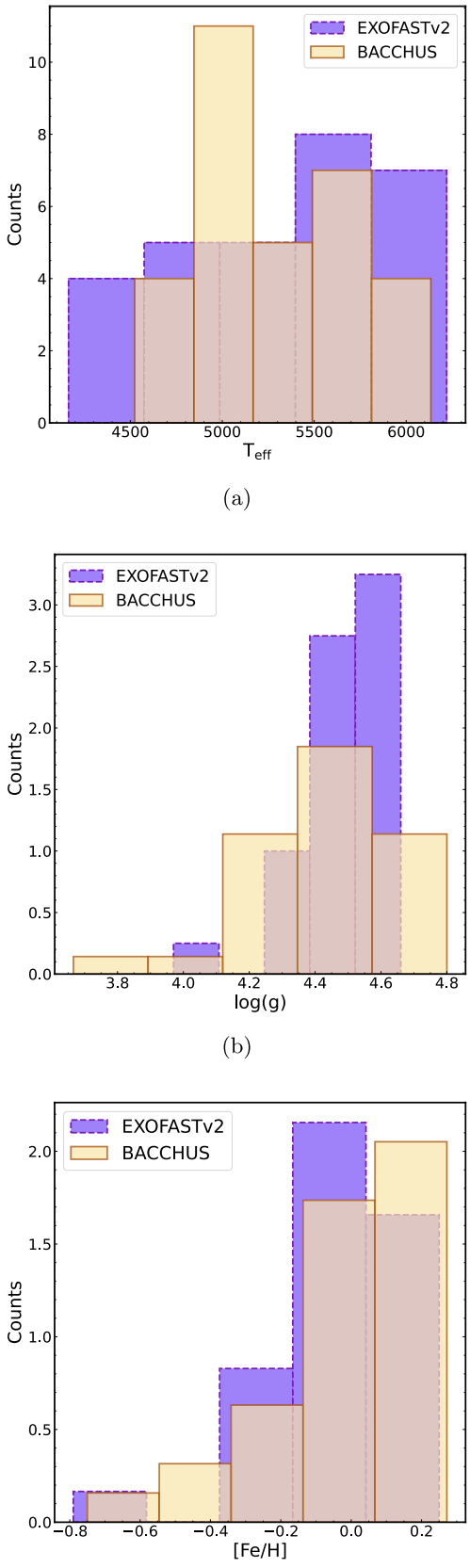


Figure 2. Histograms of the sample's (a) $T_{\rm eff}$, (b) log(g), and (c) [Fe/H] distributions for parameters from spectroscopic parameters from BACCHUS (orange; this work) and photometric parameters from EXOFASTv2 (purple).

Table 3
Spectroscopic and Photometric Stellar Parameters

Object	Spectroscopic								Photometric					
	$T_{\rm eff}$ (K)	σ_T	log(g)	$\sigma_{\log(g)}$	$v_{\rm micro}$	$\sigma v_{\rm micro}$	[Fe/H]	$\sigma_{\rm [Fe/H]}$	$T_{\rm eff}$ (K)	σ_T	log(g)	$\sigma_{\log(g)}$	[M/H]	$\sigma_{\rm [M/H]}$
HD 89744	6134	67	3.66	0.13	1.64	0.05	0.19	0.32	6210	219	3.97	0.07	0.23	0.11
HD 46588	6093	53	4.29	0.31	1.33	0.07	−0.15	0.03	6220	219	4.34	0.08	0.01	0.10
*54 Psc	5141	14	4.38	0.20	0.74	0.02	0.16	0.03	5283	133	4.52	0.05	0.16	0.11
V* HN Peg	5927	1	4.35	0.07	1.21	0.03	−0.00	0.01	6000	205	4.43	0.07	−0.01	0.10
HD 126053	5612	42	4.30	0.40	1.17	0.05	−0.38	0.02	5830	191	4.44	0.08	−0.28	0.16
GJ 417	5779	42	4.42	0.28	1.19	0.03	0.05	0.03	5490	156	4.43	0.07	0.20	0.14
HIP 9269	5493	111	4.41	0.60	1.42	0.07	0.16	0.07	6050	304	4.25	0.09	0.17	0.14
G171-58	5798	47	4.17	0.34	1.35	0.03	0.09	0.03	5720	262	4.46	0.06	−0.27	0.13
HIP 26653	5469	51	4.48	0.31	1.37	0.03	−0.06	0.03	5860	205	4.30	0.09	−0.03	0.12
HD 106888	5922	28	4.48	0.24	0.92	0.04	0.02	0.11	5480	170	4.50	0.06	0.00	0.11
HD 51400	5415	19	4.53	0.25	1.05	0.02	0.05	0.01	5570	170	4.52	0.05	0.04	0.12
HD 203030	5524	70	4.57	0.33	1.52	0.04	0.01	0.09	5750	170	4.46	0.06	−0.05	0.09
HD 8291	5686	10	4.61	0.12	0.86	0.02	−0.07	0.01	4910	255	4.62	0.04	−0.31	0.05
HD 16270	4719	29	4.27	0.48	0.62	0.04	0.24	0.09	4982	122	4.56	0.05	0.16	0.14
HD 116012	4990	39	4.69	0.62	1.06	0.03	0.08	0.10	4942	117	4.57	0.05	−0.07	0.14
BD +21 55	4820	28	4.36	0.07	0.21	0.05	−0.13	0.10	4960	124	4.56	0.04	0.25	0.28
BD +60 1417	4907	49	4.66	0.51	1.12	0.03	0.11	0.11	4452	105	4.62	0.04	−0.01	0.09
StKM 2-1777	4719	76	4.48	⋯	1.12	0.071	−0.07	0.03	5610	416	4.48	0.06	0.23	0.53
HD 253662	5280	23	4.35	0.06	0.51	0.03	0.28	0.07	5160	141	4.51	0.05	0.11	0.28
CD –24 407	5035	15	4.48	0.41	0.31	0.03	−0.01	0.10	5010	177	4.57	0.04	−0.17	0.37
BD +13 2269	5480	66	4.80	0.43	1.22	0.04	0.08	0.10	4466	113	4.62	0.04	0.24	0.33
BD +01 299	4524	37	4.26	0.85	0.78	0.10	0.12	0.18	4741	125	4.56	0.04	0.18	0.35
StKM 1-1526	4998	56	4.58	⋯	0.95	0.07	0.13	0.02	5613	141	4.58	0.05	−0.79	0.14
TYC 5213-5451	4829	20	4.70	0.17	0.67	0.03	0.04	0.03	4164	96	4.66	0.04	−0.04	0.35
LP 617-58[a]	5111	20	4.26	0.10	0.59	0.03	−0.39	0.01	5349	$^{+7.05}_{-7.34}$	4.52	$^{+0.01}_{-0.00}$	−0.23	0.00
HIP 63506	4600	97	4.54	⋯	1.06	0.08	−0.59	0.04	5289	147	4.54	0.05	−0.14	0.20
LSPM J0632+5053	5405	5	4.74	0.19	0.93	0.02	0.25	0.01	4370	102	4.65	0.04	−0.02	0.07
NLTT 1011	5006	84	4.30	⋯	1.62	0.06	−0.48	0.12	5850	212	4.30	0.09	−0.03	0.13
HD 125141	5749	78	4.49	0.57	1.28	0.04	−0.08	0.10	5570	234	4.53	0.05	−0.03	0.10
BD +06 2986	4468	106	4.61	⋯	1.00	⋯	−0.80	0.06	4543	135	4.61	0.04	0.33	0.28
BD +24 4329	4939	89	4.48	0.88	1.34	0.05	−0.17	0.09	5420	178	4.50	0.06	0.21	0.34
BD +49 2561	4959	31	4.71	0.49	0.84	0.05	0.02	0.08	4194	106	4.61	0.04	0.38	0.26

Notes. Spectroscopic [Fe/H] ≈ [M/H] is assumed when determining best-fit parameters
[a] Not converged through EXOFASTv2. Initial photometric parameters taken from Gaia DR3.

BACCHUS iteratively adjusts the parameters until it identifies the optimal combination of $T_{\rm eff}$, log(g), [M/H], and microturbulent velocity ($v_{\rm mic}$) that yields consistent abundances derived from both Fe I and Fe II lines from excitation and ionization equilibrium. For one of our coolest targets, BD +06 2986, the microturbulent velocity did not converge; as a result, we adopt a $v_{\rm mic} = 1.00$ for this target. Our final spectroscopic parameters via BACCHUS are shown in Table 3. The parameter uncertainties are estimated from the line-to-line scatter in Fe abundances, as discussed in C. R. Hayes et al. (2022).

3.2.2. Photometric versus Spectroscopic Surface Gravity

In our initial determination of the fundamental stellar parameters for the sample, we adopt the photometric surface gravity derived from EXOFASTv2 as an initial guess and solve for all parameters (effective temperature, surface gravity, metallicity, and microturbulence) with BACCHUS. For several cooler K-type stars, we find large uncertainties in the spectroscopic surface gravity (exceeding 1 dex), likely due to weak Fe II lines at lower temperatures and also the increased presence of molecular absorption features in these stars, both of which increase the line-to-line Fe II abundance scatter. For the K dwarf targets StKM 2-1777, StKM 1-1526, HIP 63506, NLTT 1011, and BD +06 2986, we therefore fix log g to the photometric value. Spectroscopic surface gravities in cool dwarfs are often poorly constrained owing to the limited number and weakness of Fe II lines (V. Neves et al. 2009; M. Tsantaki et al. 2013). As a result, enforcing ionization equilibrium can lead to unstable solutions and inflated uncertainties in the derived parameters. By fixing log g to the photometric value, we can reduce these degeneracies and obtain estimates of $T_{\rm eff}$ and [Fe/H] (G. Torres et al. 2010; D. Huber et al. 2013; A. Mortier et al. 2014). We rerun the analysis for these stars while fixing the surface gravity to the photometrically determined value. We find that fixing the surface gravity with the photometric value alleviates larger errors on other parameters as well, so we proceed to adopt this method for these stars.

3.3. Abundance Determination

Once the stellar parameters were established, we used BACCHUS to measure abundances for 11 elements. For each spectral line, the code synthesizes five model spectra with abundances spanning from –0.6 to +0.6 dex around the expected abundance, assuming a solar-scaled composition

Table 4
Element Abundances in the Solar Photosphere as Measured From N. Grevesse et al. (2007)

Element	Photospheric Abundance $(A(X)_{\odot})$
C	8.43
O	8.66
Mg	7.53
Si	7.51
Ca	6.31
Al	6.37
Fe	7.45
Y	2.21
N	7.78
S	7.14

adjusted to the star's metallicity. Abundances are then determined using four independent approaches (see details in Section 3.2.1). The final abundance for each element is taken as the mean of all lines yielding consistent (unflagged) results across these methods.

We determine abundance uncertainties by first remeasuring each star's abundance in each element eight times, each time fixing all parameters to those reported in Table 3 except for one, which we modify by first adding and then subtracting the associated uncertainty in that parameter. This process results in eight new abundances per element (four that correspond to adding the uncertainty to the modified parameter, four to subtracting) that reflect how each adopted stellar parameter affects the resulting abundance. The final abundance uncertainty we report is the quadrature sum of the average abundance difference induced by each stellar parameter's uncertainty (four terms) and also the standard error on the mean line-by-line abundance (the fifth term) (T. Bensby et al. 2014).

We use the notation outlined in J. M. Brewer & D. A. Fischer (2016) to convert from our reported [X/H], the $\log_{10}$ of the solar relative number abundance of an element with respect to hydrogen, to abundance ratios for any two given elements:

$$[X/\mathrm{H}] = A(X)_{\star} - A(X)_{\odot}, \tag{1}$$

where X denotes the element. The abundance ratios are calculated following Equation (2):

$$X_1/X_2 = 10^{([X_1/\mathrm{H}]+(X_1/\mathrm{H})_{\odot})-([X_2/\mathrm{H}]+(X_2/\mathrm{H})_{\odot})}. \tag{2}$$

We adopt solar abundances from N. Grevesse et al. (2007) (see Table 4).

We use the following formula from N. R. Hinkel et al. (2022) to determine the error for our abundance ratios:

$$\delta\frac{\mathrm{X_1}}{\mathrm{X_2}} = \ln(10)\sqrt{\delta[X_1/\mathrm{H}]_*^2 + \delta[X_2/\mathrm{H}]_*^2}\,. \tag{3}$$

To propagate the error for [Y/Mg], we use the following formula:

$$\sigma_{[\mathrm{Y/Mg}]} = \sqrt{\sigma^2_{[\mathrm{Y/H}]} + \sigma^2_{[\mathrm{Mg/H}]}}\,.$$

We report the resulting ratios in Table 8.

Our different resolution modes (R = 50,000 or R = 130,000) affect our parameters, abundances, and abundance ratio precision. We find the following precision for R = 130,000 data: 0.03 dex for [Fe/H] and 0.11 for C/O ratios. For the 50,000 data, we find the following: 0.03 dex for [Fe/H] and 0.08 for C/O. We find a higher precision for the R = 50,000 data for the C/O abundance ratio, which we attribute to the higher average $\langle \mathrm{S/N} \rangle > 500$ for this resolution (M. Bedell et al. 2014; P. E. Nissen 2015).

3.3.1. Line Selection

We adopt version 5 of the Gaia-ESO line list for our atomic transition data (U. Heiter et al. 2021) and combine molecular transition data from numerous sources. Our line selections are initially from the NIST database (Y. Ralchenko & A. Kramida 2020; A. Kramida et al. 2023). We follow J. R. Kolecki & J. Wang (2022) and restrict our line choices to those that have a transition strength accuracy value of "C" or better. We have a final line selection from referencing line lists from Gaia-ESO (U. Heiter et al. 2021), the solar spectrum (C. E. Moore et al. 1966), and C. E. Mack et al. (2018), J. R. Kolecki & J. Wang (2022), and C. L. Phillips et al. (2024). We use different line selections curated for our two observing mode configurations: (A) CD III and CD VI, and (B) CD II and CD VI (Table 1). The main observing mode for our sample is with (A) CD III and CD VI, which covers wavelengths 4800−5441 Å and 7410−9140 Å, respectively. Our line list for configuration A is composed of the following: 18 Ti I lines, 16 C I and C_2 lines, 3 O I lines, 20 Mg I lines, 27 Si I lines, 7 CN lines (for nitrogen), 6 Ca I lines, 4 Ca II lines, 6 Al I lines, 13 Y I and Y II lines, 2 S I lines, and 111 Fe I and Fe II lines.

Three targets were observed in configuration B, which covers wavelengths 4265−4800 Å and 7410−9140 Å. Our line list for configuration B is composed of the following: 11 Ti I lines, 6 C I lines, 3 O I lines, 21 Mg I lines, 27 Si I lines, 2 S I lines, 4 CN lines (for nitrogen), 4 Ca I lines, 2 Ca II lines, 6 Al I lines, 7 Y I and Y II lines, 70 Fe I and Fe II lines.

3.3.2. Carbon Abundance

Our coolest K-type stars (StKM 2-1777, StKM 1-1526, HIP 63506, NLTT 1011, BD +06 2986, and BD +24 4329) are riddled with molecular features and have weak atomic carbon lines. As a result of this, we turn to a set of C_2 swan lines to determine the carbon abundance of these stars (J. S. A. Brooke et al. 2013; T. Ryabchikova et al. 2015, 2022). We use the following carbon C I lines for our hotter stars: 4932.0, 5021.1, 5380.3, 8058.6, 8335.1, 8727.1, and 9061.4 Å. For the cooler stars we use the following C_2 lines: 5151.8, 5153.1, 5156.5, 5159.4, 5126.0, 5130.4, 5132.6, 5135.5, 5146.0, and 5149.1 Å.

The difficulty in measuring C and O makes determining these C/O ratios significantly challenging. Future high-resolution near-infrared (NIR) spectroscopy of our coolest targets from IGRINS ($R \sim 45{,}000$) would prove beneficial for accessing CO and OH features to calculate C/O ratios (N. Hejazi et al. 2024).

3.3.3. Nitrogen Abundance

Measuring N from optical spectra is difficult because there are no reliable atomic N lines in this wavelength regime (see discussion in, e.g., G. Tautvaišienė et al. 2015; G. Casali et al. 2019). As such, using CN molecules is our only option. To determine the nitrogen abundance from CN molecular features, the carbon abundance was determined using the methods described in the previous subsection and then fixed for each star prior to the nitrogen determination. For stars that have uncertain carbon measurements and resulting upper limits

Table 5
Known Sun Parameters versus Spectroscopic Parameters Found for the Sun from BACCHUS Using PEPSI Data

Parameter	$\text{Sun}_{\odot}$	$\text{Sun}_{\text{BACCHUS}}$
T_{eff}	5774	5710 ± 11
log(*g*)	4.44	4.41 ± 0.22
[Fe/H]	0.00	−0.00 ± 0.01

(see Section 3.3.4), we omit nitrogen abundance determination.

3.3.4. Upper Limits on Abundances and Abundance Ratios

For some of our coolest K dwarfs with weak lines, we are only able to report upper limits on abundances and resulting abundance ratios. To determine the upper limit on a given abundance, we first check that the BACCHUS fit is adequate and adopt the upper limit on A_{syn} for a given element (e.g., Z. Hackshaw et al. 2025). We describe our findings for NLTT 1011, HIP 63506, BD +06 2986, BD +24 4329, StKM 1-1526, StKM 2-1777, and HD 116012.

For NLTT 1011 (K7), there is an O detection at the O I λ7771.9 line. We find an upper limit on [O/H] = −0.85, which leads to a reported C/O > 0.76. There are two Ca detections at Ca I $\lambda\lambda$4847.3 and 5260.4, which leads to a reported Ca/Al < 1.8. There are two Y detections at Y II $\lambda\lambda$4900.1 and 5087.4. We find an average upper limit of [Y/H] = −0.77 and [Y/Mg] < −0.314.

We find that for HIP 63506 (K6V) there are no O or C detections, and therefore we cannot place an upper limit on the C/O ratio. There are two Y detections at Y II $\lambda\lambda$4900.1 and 5087.4 for NLTT 1011. We find an average upper limit of [Y/H] = −1.02 and [Y/Mg] < −0.54.

There are no usable O and C lines for BD +06 2986, so we cannot constrain or place an upper limit on the C/O ratio. There are two Y detections at Y I $\lambda\lambda$4643.7 and 4674.8. We find an average upper limit of [Y/H] = −1.11 and [Y/Mg] < −0.687.

BD +24 4329 (K6) has one C detection at C I λ8335.1. [C/H] has an upper limit of −1.17, with leads to a C/O < 1.79. We use two Ca detections at Ca II $\lambda\lambda$8248.8 and 8912.2 and find an upper limit of [Ca/H] = −0.79, leading to Ca/Al < 1.37.

StKM 1-1526 (K4/5) has two C detections at C_2 $\lambda\lambda$4932.0 and 5380.3. This results in an upper limit on [C/H] = −1.94 and C/O > 1.04 for StKM 1-1526. StKM 2-1777 (K5) has only one C detection at C I λ5149.1. We find an upper limit on [C/H] = −2.67 and a C/O > 1.005. HD 116012 has two Y detections at Y II $\lambda\lambda$4883.1, 5087.4, and 5289.8, with an upper limit average for [Y/H] = −0.78, leading to [Y/Mg] < −0.94.

3.3.5. NLTE Effects

In this work, we calculate the 1D non-LTE (NLTE) oxygen abundances for our sample by applying correction factors. NLTE effects are known to be a cause of abundance offsets and can require abundance corrections >0.1 dex (e.g., P. Jofré et al. 2019). We use NLTE correction lookup tables from the Max Planck Institute for O I (T. M. Sitnova et al. 2013).[18] We use the spectroscopic parameters (Table 3) found with BACCHUS as input stellar parameters and the plane-parallel 1D MAFAGS-OS. We find the mean NLTE oxygen for the O triplet lines and apply this to our [O/H] to determine the NLTE [O/H] abundance. We provide the oxygen corrections in Table B1.

[18] https://gemini-web.mpia.de/gui-siuAC_secEnew.php

Table 6
Stellar Abundances and Ratios for the Sun from BACCHUS

Property	$\text{Sun}_{\text{BACCHUS}}$
[Fe/H]	−0.00 ± 0.01 dex
[C/H]	0.08 ± 0.09 dex
$[\text{O/H}]_{\text{NLTE}}$	0.18 ± 0.06 dex
[Mg/H]	0.01 ± 0.02 dex
[Si/H]	−0.03 ± 0.07 dex
[Ca/H]	0.11 ± 0.09 dex
[Al/H]	−0.01 ± 0.03 dex
[N/H]	0.10 ± 0.03 dex
[Y/H]	−0.22 ± 0.11 dex
[Ti/H]	−0.07 ± 0.05 dex
[S/H]	0.20 ± 0.19 dex
C/O	0.53
Mg/Si	1.14

4. Validating Results

4.1. Testing BACCHUS with a Solar Spectrum from PEPSI

To calibrate and test our line list, derived stellar parameters, and methodology (Section 3.3), we anchor our analysis with the Sun as seen from PEPSI. We test the Sun to derive the ratios [O/H], [C/H], [S/H], [N/H], [Mg/H], [Si/H], [Ca/H], and [Y/H], and we derive C/O and Mg/Si ratios to compare to literature values (N. Grevesse et al. 2007; M. Asplund et al. 2009). BACCHUS has been used in recent abundance and parameter estimation for stellar hosts of directly imaged planets and brown dwarfs (Z. Zhang et al. 2023, 2025b; A. Rothermich et al. 2026). To test the validity of our method and the BACCHUS code with data from PEPSI, we use observations of the Sun taken with PEPSI from K. G. Strassmeier et al. (2018a). These solar observations were taken in R = 250,000 mode, so we must convolve them down to the resolution of our observations before proceeding with BACCHUS. We use a 1D-Gaussian kernel to convolve down to the resolution of most of our data, R = 130,000. In K. G. Strassmeier et al. (2018a), the Sun was observed across all CDs (CD I−CD VI); we take the Sun's spectrum with PEPSI and reduce to just CD III and CD VI to test BACCHUS, as this is the dominant cross-disperser configuration for our sample.

Generally we find good agreement between our spectroscopic parameters found for the Sun with BACCHUS and M. Asplund et al. (2009). We note that the largest discrepancy appears between T_{eff}, where we find a lower T_{eff} by about ∼50 K (Table 5).

From our line selection, we find nonzero systemic offsets between expected and measured [X/H] values for a few elements, with the biggest discrepancy in yttrium, oxygen, and sulfur for the Sun when compared to N. Grevesse et al. (2007) (Table 4). In general, BACCHUS achieves good fits to the PEPSI solar spectrum (see Figure A1 in Appendix A), so it is likely that the discrepancies come from issues with the line list

or the spectral synthesis method rather than from data quality. Systematic abundance differences between surveys are common and remain an open issue in high-resolution spectroscopy. These offsets can arise from differences in adopted atomic data (e.g., laboratory values vs. empirically tuned oscillator strengths), unidentified or imperfectly modeled blends, the use of 1D rather than 3D model atmospheres, and residual NLTE effects (H. Socas-Navarro 2015; J. M. Brewer et al. 2016; M. Bergemann et al. 2021; M. Zhang et al. 2024; A. G. M. Pietrow et al. 2026).

When reporting BACCHUS abundances for other stars in the format [X/H], we are implicitly normalizing the abundances to the solar values. Therefore, we can use the observed offsets in solar abundances from Table 6 to correct the BACCHUS-reported stellar abundances and bring them in line with the BACCHUS-determined solar abundance values (Equation (4)). We calculate an [Fe/H] $= -0.00 \pm 0.01$ for the Sun, so we do not apply a correction for the sample for [Fe/H]. In what follows, we subtract these solar correction factors from the BACCHUS abundances in Table 6 to determine final solar-normalized [X/H] abundances in Table 7:

$$[X/\mathrm{H}] = ((A(X)_{\star} - A(X)_{\odot}) - [X/\mathrm{H}]_{\odot,\mathrm{PEPSI}}, \quad (4)$$

where X denotes the element.

4.2. Comparison to Brewer Catalog and M. Rice & J. M. Brewer (2020)

Five stars in our sample (HD 46588, HD 203030, HD 126053, GJ 417, and HD 37216) were previously observed as part of the J. M. Brewer & D. A. Fischer (2016) study within the California Planet Search (CPS) program (hereafter Brewer Catalog), as well as one star, *54 Psc, from M. Rice & J. M. Brewer (2020). Observations were carried out using the HIRES spectrograph on the Keck I telescope ($R \sim 70{,}000$) with a typical signal-to-noise ratio (SNR) of approximately 100. The resulting spectra were analyzed in a uniform manner employing the *Spectroscopy Made Easy* (SME; J. A. Valenti & N. Piskunov 1996) package, which provided precise determinations of fundamental stellar parameters (e.g., $T_{\rm eff}$, log(g), and $v \sin i$) and elemental abundances for 15 species, utilizing atomic data from the Vienna Atomic Line Database (VALD-3). Species measured in the Brewer Catalog include C, N, O, Na, Mg, Al, Si, Ca, Ti, V, Cr, Mn, Fe, Ni, and Y. The following species from the Brewer Catalog are used in this work: C, N, O, Mg, Al, Si, Ca, Ti, Fe, and Y (see Section 5).

For the five stars in J. M. Brewer et al. (2016), we find generally good agreement between our abundances derived from BACCHUS and those from the Brewer Catalog (Figures 3 and 4). We note a systematic offset of [O/H] and [Y/H]. In J. M. Brewer et al. (2016), NLTE corrections were not applied to their sample. However, we note that the original discrepancy for [O/H] and [Y/H] is caused by an offset from the PEPSI data, as discussed in Section 4.1. Two of our stars, HD 46588 and HD 37216, have the biggest offset in [N/H] and [O/H], where our values are subsolar compared to the near-solar values from J. M. Brewer et al. (2016). For *54 Psc, we find close agreement between our abundance values and M. Rice & J. M. Brewer (2020), with the most notable offset for the [N/H] abundance (Figure 4).

J. M. Brewer et al. (2016) use 12 OH and O I lines and seven nitrogen lines (J. M. Brewer, private communication) in addition to the molecular lines (CN) and do not use any NLTE corrections for oxygen. The Brewer Catalog and M. Rice & J. M. Brewer (2020) differ from BACCHUS in several ways, including atomic data source; determination of $T_{\rm eff}$, log$g$, and [Fe/H]; and microturbulence determination and abundance determination methodology. These various factors can impact our final abundance determination.

Typical uncertainties in the stellar parameters derived from the J. M. Brewer et al. (2016) catalog are on the order of ∼60 K in effective temperature, ∼0.15 dex in surface gravity, and ∼0.06 dex in metallicity. For HD 203030, $T_{\rm eff} = 5441 \pm 60$ K, log(g) $= 4.51 \pm 0.15$, and [Fe/H] $= 0.08 \pm 0.06$ (J. M. Brewer et al. 2016). Our values for HD 203030 are $T_{\rm eff} = 5524 \pm 70$ K, log$g = 4.57 \pm 0.33$, and [Fe/H] $= 0.01 \pm 0.09$. For HD 46588 from the Brewer Catalog, $T_{\rm eff} = 6145 \pm 60$ K, log(g) $= 4.30 \pm 0.15$, and [Fe/H] $= -0.05 \pm 0.06$. Our values for HD 46588 are $T_{\rm eff} = 6093 \pm 53$ K, log$g = 4.29 \pm 0.31$, and [Fe/H] $= -0.03 \pm 0.03$. HD 126053 has $T_{\rm eff} = 5714 \pm 60$ K, log(g) $= 4.54 \pm 0.15$, and [Fe/H] $= -0.35 \pm 0.06$ from the Brewer Catalog, and our values are $T_{\rm eff} = 5612 \pm 42$ K, log(g) $= 4.30 \pm 0.40$, and [Fe/H] $= -0.38 \pm 0.02$. Lastly, from the Brewer Catalog for GJ 417, $T_{\rm eff} = 5905 \pm 60$ K, log(g) $= 4.47 \pm 0.15$, and [Fe/H] $= 0.16 \pm 0.06$, and our values are $T_{\rm eff} = 5779 \pm 42$ K, log(g) $= 4.42 \pm 0.28$, and [Fe/H] $= 0.05 \pm 0.03$.

In Figure 5, we show abundance ratios for C/O, Mg/Si, Ca/Al, and [Fe/H] (metallicity) for our host stars and the local solar neighborhood from J. M. Brewer et al. (2016), following restrictions in E. Calamari et al. (2024). This comparison places our sample in the broader chemical context of nearby FGK stars analyzed in a homogeneous manner. This result highlights the spread in abundance ratios for our sample and the solar neighborhood. The distributions demonstrate that our host stars span a range in chemical abundances comparable to that of the solar neighborhood population, encompassing both subsolar and supersolar metallicities, alongside a wide dispersion in C/O and Mg/Si ratios. Our host stars predominantly occupy the central region of the solar neighborhood distribution, suggesting that they are chemically typical of nearby stars rather than representing extreme deviations or a chemically peculiar set. We note that when our sample deviates from other solar neighborhood values of J. M. Brewer et al. (2016), we begin to see an increase in the error bars on our ratios, mainly the C/O and Mg/Si ratios. Our determined Mg/Si and C/O are closer to solar values than our Ca/Al values.

4.2.1. C/O and Mg/Si from Brewer Catalog

We use uncertainties and parameters found from J. M. Brewer et al. (2016), where uncertainties in the C/O values are ±10% and those in the Mg/Si values are ±3.3%. We find the following in J. M. Brewer & D. A. Fischer (2016): HD 203030 has a reported C/O $= 0.45 \pm 0.04$ and Mg/Si $= 0.95 \pm 0.03$, HD 126053 has a C/O $= 0.41 \pm 0.04$ and Mg/Si $= 1.04 \pm 0.03$, and GJ 417 (HD 97334) has a C/O $= 0.50 \pm 0.05$ and Mg/Si $= 0.98 \pm 0.03$. From our analysis our Mg/Si ratio for HD 203030 is within 1σ of the Brewer Catalog (1.14 ± 0.08 vs. 0.98). We find that HD 126053 has a Mg/Si $= 1.09 \pm 0.07$, which is very close to the Brewer Catalog value (1.04 ± 0.03). Similarly, our derived Mg/Si for GJ 417 agrees within uncertainties. Our derived C/O ratios for

Table 7
Stellar Abundances and Uncertainties for the PEPSI Sample

Object	[C/H]	[O/H]	$[O/H]_{NLTE}$	[Ca/H]	[Al/H]	[Mg/H]	[Si/H]	[Y/H]	[S/H]	[N/H]	[Ti/H]
HD 89744	0.04 ± 0.09	0.31 ± 0.13	−0.00 ± 0.11	0.09 ± 0.07	0.18 ± 0.03	0.11 ± 0.44	0.24 ± 0.19	0.08 ± 0.05	0.17 ± 0.18	0.18 ± 0.03	0.12 ± 0.06
HD 46588	−0.07 ± 0.10	−0.00 ± 0.13	−0.10 ± 0.13	−0.18 ± 0.06	−0.13 ± 0.05	−0.13 ± 0.03	−0.12 ± 0.05	−0.14 ± 0.14	−0.10 ± 0.19	−0.11 ± 0.07	−0.10 ± 0.08
*54 Psc	0.13 ± 0.13	0.14 ± 0.07	0.11 ± 0.07	0.13 ± 0.07	0.23 ± 0.05	0.23 ± 0.02	0.14 ± 0.19	0.06 ± 0.09	−0.02 ± 0.09	0.43 ± 0.17	0.23 ± 0.06
V* HN Peg	−0.01 ± 0.08	0.00 ± 0.03	−0.09 ± 0.03	0.04 ± 0.06	−0.13 ± 0.02	−0.08 ± 0.03	−0.19 ± 0.05	0.03 ± 0.06	−0.07 ± 0.13	0.01 ± 0.01	0.02 ± 0.02
HD 126053	−0.37 ± 0.13	−0.27 ± 0.12	−0.23 ± 0.12	−0.33 ± 0.07	−0.23 ± 0.03	−0.28 ± 0.03	−0.30 ± 0.06	−0.47 ± 0.18	−0.30 ± 0.23	−0.43 ± 0.04	−0.28 ± 0.08
GJ 417	0.05 ± 0.09	0.20 ± 0.14	0.13 ± 0.14	0.13 ± 0.07	0.09 ± 0.05	0.00 ± 0.03	0.11 ± 0.04	0.13 ± 0.13	−0.10 ± 0.08	0.01 ± 0.00	0.12 ± 0.07
HIP 9269	0.07 ± 0.27	−0.02 ± 0.28	−0.07 ± 0.28	0.06 ± 0.19	0.28 ± 0.09	0.21 ± 0.07	0.07 ± 0.13	−0.06 ± 0.17	−0.12 ± 0.27	0.33 ± 0.09	0.18 ± 0.16
G171-58	0.23 ± 0.13	0.33 ± 0.17	0.22 ± 0.17	0.22 ± 0.15	0.21 ± 0.03	0.15 ± 0.03	0.10 ± 0.07	0.03 ± 0.12	0.17 ± 0.09	0.32 ± 0.08	0.07 ± 0.08
HIP 26653	−0.22 ± 0.25	−0.21 ± 0.14	−0.18 ± 0.14	−0.12 ± 0.08	−0.07 ± 0.04	−0.05 ± 0.02	−0.17 ± 0.09	−0.12 ± 0.13	−0.40 ± 0.16	−0.01 ± 0.06	−0.03 ± 0.07
HD 106888	0.16 ± 0.10	0.41 ± 0.07	0.33 ± 0.07	0.00 ± 0.07	0.06 ± 0.08	−0.01 ± 0.03	0.03 ± 0.05	0.12 ± 0.10	0.05 ± 0.05	0.05 ± 0.04	0.11 0.07
HD 51400	−0.11 ± 0.18	−0.08 ± 0.09	−0.11 ± 0.09	0.06 ± 0.08	0.09 ± 0.06	0.00 ± 0. 02	0.00 ± 0.07	0.04 ± 0.1	0.06 ± 0.25	0.16 ± 0.02	0.08 ± 0.06
HD 203030	−0.15 ± 0.22	−0.06 ± 0.12	−0.10 ± 0.12	0.05 ± 0.04	−0.02 ± 0.05	0.00 ± 0.03	0.00 ± 0.07	0.10 ± 0.16	−0.20 ± 0.16	−0.07 ± 0.17	0.03 ± 0.08
HD 8291	−0.11 ± 0.08	−0.02 ± 0.04	−0.06 ± 0.04	0.00 ± 0.09	−0.08 ± 0.05	−0.12 ± 0.03	−0.07 ± 0.06	0.04 ± 0.06	−0.03 ± 0.08	−0.03 ± 0.05	−0.02 ± 0.03
HD 16270	0.26 ± 0.08	0.17 ± 0.16	0.15 ± 0.16	0.15 ± 0.20	0.27 ± 0.07	0.18 ± 0.05	0.16 ± 0.17	0.19 ± 0.2	…	0.28 ± 0.19	0.24 ± 0.18
HD 116012	0.16 ± 0.07	−0.06 ± 0.23	−0.07 ± 0.23	0.03 ± 0.14	0.22 ± 0.07	0.16 ± 0.03	0.09 ± 0.18	−0.78[a]	−0.16 ± 0.29	−0.04 ± 0.17	0.09 ± 0.16
BD +21 55	−0.29 ± 0.18	0.00 ± 0.05	−0.00 ± 0.05	−0.11 ± 0.08	−0.02 ± 0.06	−0.08 ± 0.03	−0.08 ± 0.05	−0.19 ± 0.75	−0.04 ± 0.04	0.14 ± 0.04	−0.04 ± 0.03
BD +60 1417	0.17 ± 0.06	0.34 ± 0.2	0.33 ± 0.2	0.12 ± 0.12	0.08 ± 0.07	0.07 ± 0.09	0.17 ± 0.14	0.21 ± 0.24	…	−0.22 ± 0.03	0.06 ± 0.08
StKM 2-1777	−2.57[a]	−0.29 ± 0.16	−0.31 ± 0.16	−0.51 ± 0.11	0.09 ± 0.04	−0.11 ± 0.02	−0.33 ± 0.09	0.03 ± 0.07	…	…	−0.03 ± 0.10
HD 253662	0.21 ± 0.04	0.46 ± 0.03	0.43 ± 0.03	0.36 ± 0.10	0.34 ± 0.04	0.31 ± 0.02	0.36 ± 0.06	0.31 ± 0.01	0.33 ± 0.03	0.35 ± 0.03	0.36 ± 0.05
CD –24 407	−0.05 ± 0.23	0.12 ± 0.18	0.10 ± 0.18	0.03 ± 0.12	0.08 ± 0.06	0.04 ± 0.03	0.11 ± 0.12	−0.03 ± 0.22	0.12 ± 0.19	0.10 ± 0.10	0.09 ± 0.13
BD +13 2269	−0.14 ± 0.23	0.00 ± 0.15	−0.02 ± 0.15	0.19 ± 0.09	0.08 ± 0.06	0.07 ± 0.04	0.11 ± 0.07	0.19 ± 0.16	0.01 ± 0.27	0.21 ± 0.10	0.13 ± 0.06
BD +01 299	0.03 ± 0.17	−0.12 ± 0.18	−0.13 ± 0.18	0.02 ± 0.3	0.09 ± 0.06	−0.06 ± 0.23	−0.08 ± 0.34	0.00 ± 0.22	…	0.19 ± 0.40	0.21 ± 0.24
StKM 1-1526	−1.94[a]	−0.40 ± 0.08	−0.43 ± 0.08	−0.31 ± 0.10	−0.39 ± 0.04	0.18 ± 0.02	0.03 ± 0.08	0.12 ± 0.02	…	…	0.11 ± 0.07
TYC 5213-545-1	0.12 ± 0.05	0.05 ± 0.06	0.04 ± 0.06	−0.02 ± 0.14	−0.04 ± 0.06	0.03 ± 0.04	0.05 ± 0.08	0.04 ± 0.11	…	−0.15 ± 0.07	0.12 ± 0.06
LP 617-58	−0.28 ± 0.06	−0.15 ± 0.04	−0.17 ± 0.04	−0.28 ± 0.07	−0.09 ± 0.03	−0.05 ± 0.01	−0.21 ± 0.05	−0.48 ± 0.07	…	0.83 ± 0.05	−0.08 ± 0.04
HIP 63506	…	…	…	−0.02 ± 0.08	−0.29 ± 0.04	−0.47 ± 0.05	−0.64 ± 0.09	−1.02[a]	…	…	−0.45 ± 0.15
LSPM J0632+5053	0.17 ± 0.16	0.17 ± 0.06	0.14 ± 0.06	0.23 ± 0.07	0.25 ± 0.06	0.19 ± 0.02	0.27 ± 0.06	0.34 ± 0.09	0.26 ± 0.19	0.27 ± 0.04	0.34 ± 0.09
NLTT 1011	0.25 ± 0.22	−0.86[a]	−0.85[a]	−0.82[a]	−0.00 ± 0.06	−0.45 ± 0.02	−0.77[a]	…	…	…	−0.65 ± 0.32
HD 125141	0.00 ± 0.18	0.03 ± 0.23	−0.01 ± 0.23	0.00 ± 0.11	0.06 ± 0.04	−0.10 ± 0.05	0.02 ± 0.05	−0.13 ± 0.23	−0.27 ± 0.21	−0.00 ± 0.09	−0.07 ± 0.13
BD +06 2986	…	…	…	0.22 ± 0.16	−0.27 ± 0.08	−0.41 ± 0.08	−0.72 ± 0.17	−0.40 ± 0.05	…	−0.64 ± 0.13	−0.50 ± 0.10
BD +24 4329	−1.17[a]	−0.84 ± 0.46	−0.85 ± 0.46	−0.79[a]	0.10 ± 0.07	−0.17 ± 0.14	−0.38 ± 0.36	−0.26 ± 0.4	…	…	0.40 ± 0.16
BD +49 2561	0.02 ± 0.15	0.02 ± 0.20	0.01 ± 0.20	−0.00 ± 0.09	0.04 ± 0.06	0.01 ± 0.07	0.05 ± 0.18	0.06 ± 0.17	−0.11 ± 0.34	−0.23 ± 0.15	0.15 ± 0.15

Note.
[a] Upper limit.

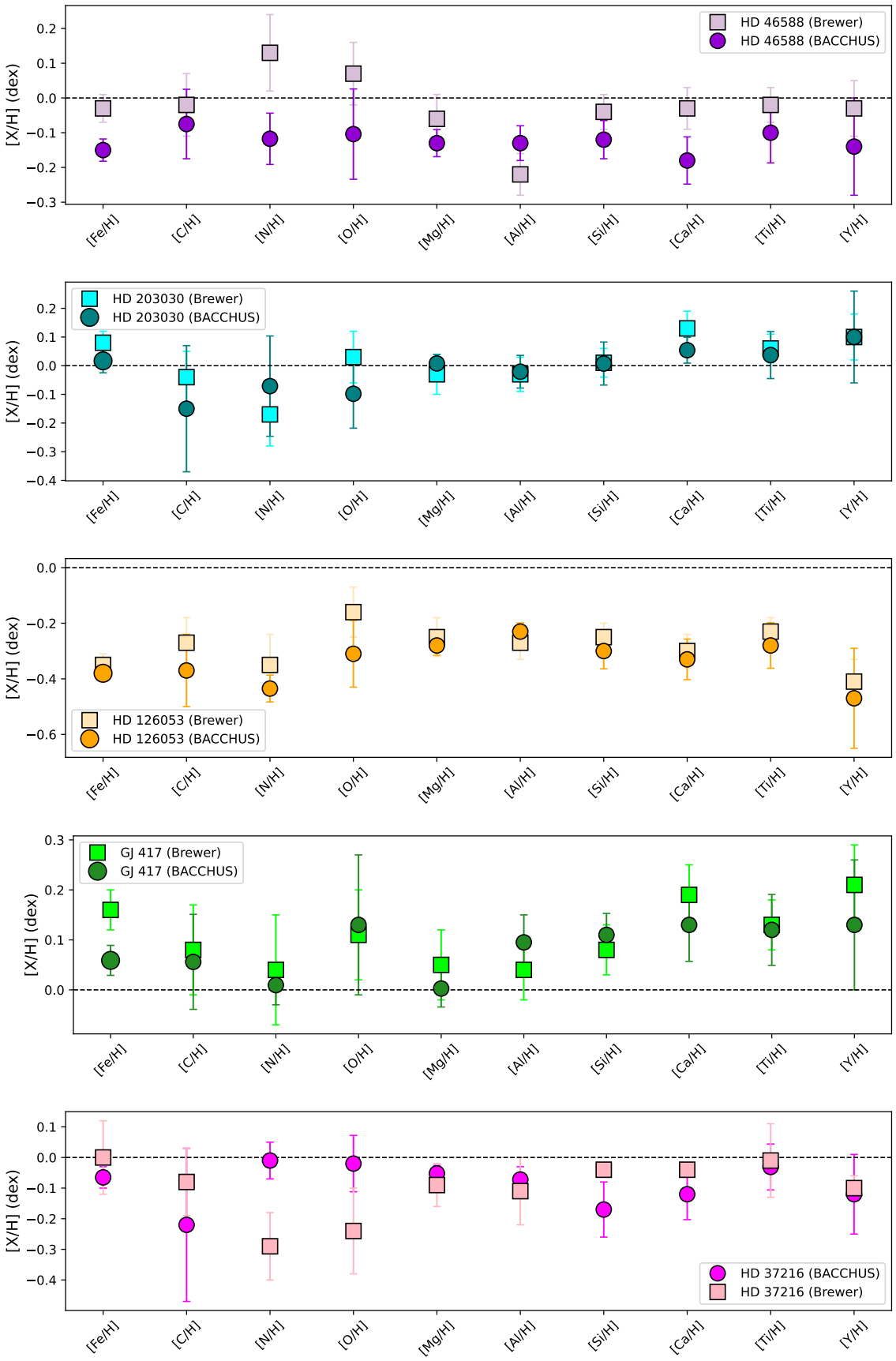


Figure 3. Elemental abundances for HD 46588 (purple; top panel) from BACCHUS (circles) and from J. M. Brewer et al. (2016) (squares) and their associated errors. Remaining panels are for HD 203030 (blue), HD 126053 (orange), GJ 417 (green), and HD 37216 (pink).

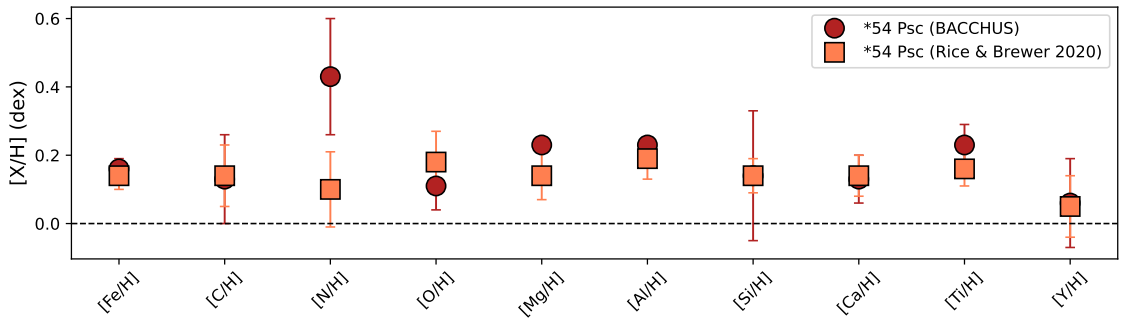


Figure 4. Same as Figure 3, but abundances for *54 Psc from BACCHUS (red circles) and M. Rice & J. M. Brewer (2020) (orange squares).

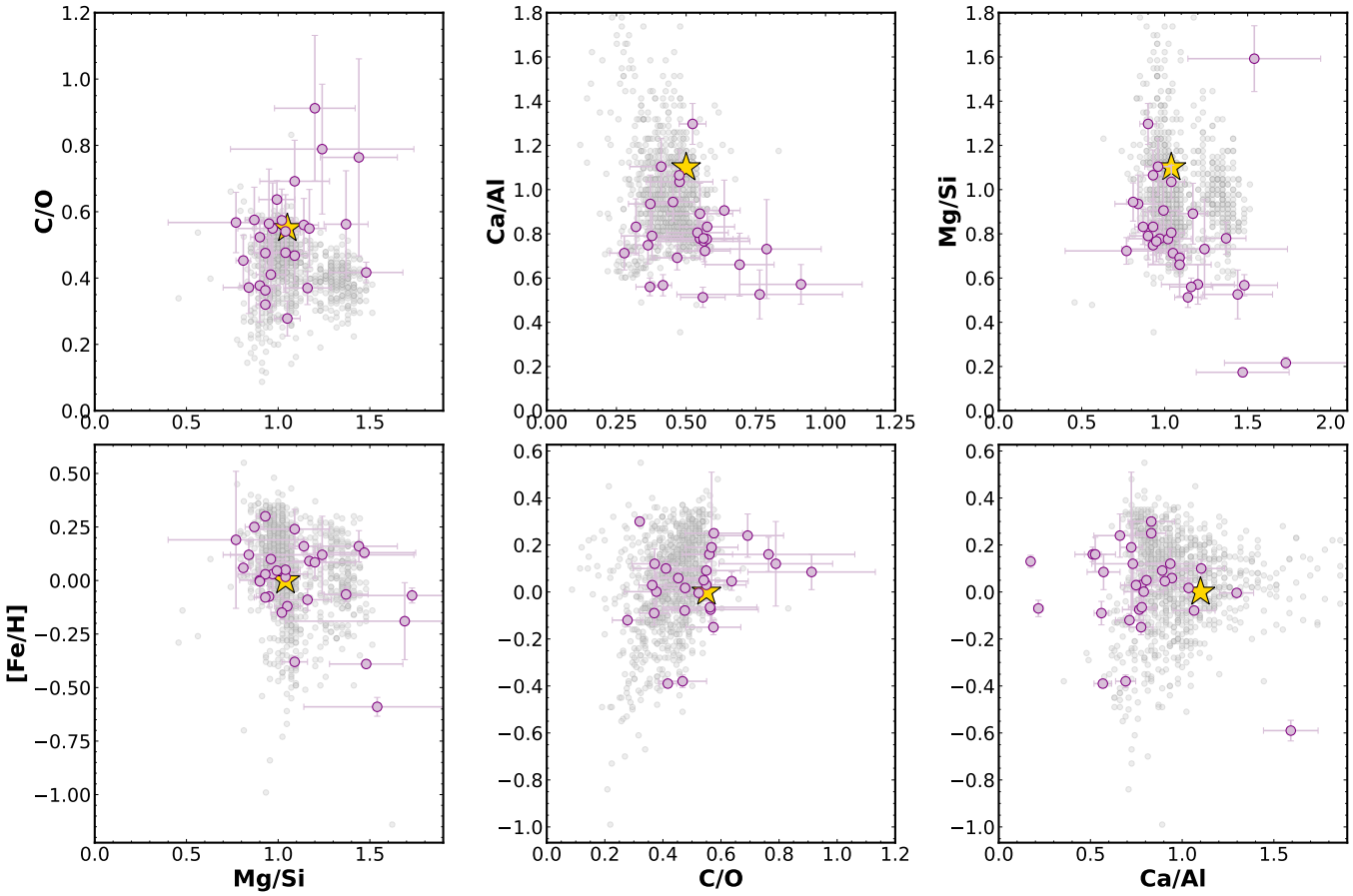


Figure 5. Abundance ratios of stars in the solar neighborhood from J. M. Brewer et al. (2016) and J. M. Brewer & D. A. Fischer (2016), plotted following Figure 1 from E. Calamari et al. (2024) with our PEPSI sample (purple points) overlaid from Table 1. The Sun's values are marked with a gold star (N. Grevesse et al. 2007).

HD 203030, HD 126053, and GJ 417 are within 1σ of the Brewer Catalog.

4.3. Comparison to Literature

We examine the literature for our sample that was not examined in J. M. Brewer & D. A. Fischer (2016) and M. Rice & J. M. Brewer (2020). We focus on stars with previously reported C/O and Mg/Si measurements, and below we highlight a few examples.

In R. E. Luck (2017, 2018), abundances for carbon, oxygen, magnesium, and silicon are presented for V_* HN Peg and HIP 9269 (HD 12051) with the Sandiford spectrograph and the Hobby–Eberly telescope at the McDonald Observatory. The spectral lines used to determine C/O were C I at 5052 and 5380 Å, C_2, O I at 6155 Å, and [O I] at 6300 Å—where LTE is assumed. For V^* HN Peg, [C/H] $= -0.10 \pm 0.09$ and [O/H] $= 0.07 \pm 0.09$, which leads to a C/O $= 0.37 \pm 0.03$ using solar normalizations taken from M. Asplund et al. (2009). This value is lower than our C/O of 0.52 ± 0.04 from BACCHUS. The [Mg/H] and [Si/H] are 0.10 ± 0.02 and 0.05 ± 0.01, respectively, leading to Mg/Si $= 1.38 \pm 0.22$, which is higher than our Mg/Si $= 0.90 \pm 0.05$. The [Fe/H] of 0.01 ± 0.01 matches our values of 0.00 ± 0.01. The $T_{\rm eff} = 5972.0$ K from R. E. Luck (2017) is close to our value of 5927 ± 1 K.

HIP 9269 has a C/O value of 0.40, from $\langle$C$\rangle = 8.58$ and $\langle$O$\rangle = 8.98$ compared to our C/O value of 0.76 ± 0.29, a 2σ difference. The [Mg/H] $= 0.37 \pm 0.07$ and [Si/H] $= 0.30 \pm 0.06$, which leads to a Mg/Si $= 1.44 \pm 0.13$ (R. E. Luck 2017). This is in line with our Mg/Si value for HIP 9269 of 1.44 ± 0.21. The [Fe/H] $= 0.24 \pm 0.04$

(R. E. Luck 2017) is within 1σ of our value for [Fe/H], which is 0.16 ± 0.07.

HD 89744 has multiple prior determinations of its atmospheric parameters reported in the literature, along with C/O and Mg/Si ratios (E. Delgado Mena et al. 2010). E. Delgado Mena et al. (2010) find stellar parameters of $T_{\rm eff} = 6234$ K, $\log(g) = 3.98$, and [Fe/H] = 0.22. They also find [O/H] = 0.00, [C/H] = 0.17, [Mg/H] = 0.16, and [Si/H] = 0.26. The most recent findings with MOOG in B. M. Morris et al. (2019) show $T_{\rm eff} = 6070 \pm 110$, $\log(g)$ 4.18 ± 0.05, and [Fe/H] = 0.26. Our stellar parameters are within 2σ for $T_{\rm eff}$ and [Fe/H]. E. Delgado Mena et al. (2010) report a C/O ratio of 0.98 and Mg/Si ratio of 0.85, a notable contrast to our derived C/O = 0.54 but within 1σ for our derived Mg/Si $= 0.77 \pm 0.37$. There is a lack of literature information on how these ratios were determined, making exact comparisons difficult.

BD +13 2269 has few literature measurements of its stellar parameters. The most recent stellar parameter and abundance measurements for BD + 13 2269 are presented in A. Rothermich et al. (2024), W. Zong et al. (2020), and R. Wang et al. (2020). $T_{\rm eff}$, $\log(g)$, and 11 elements were measured from the Large Sky Area Multi-Object Fiber Spectroscopic Telescope (LAMOST) Medium Resolution ($R \sim 7500$) Survey datasets with a machine learning method. R. Wang et al. (2020) and W. Zong et al. (2020) found $T_{\rm eff} = 5542$, $\log(g) = 4.60$, [Fe/H] $= 0.22 \pm 0.01$, C/O = 1.40, and Mg/Si = 0.79. The previous [Fe/H] measurements are about 2σ from our measured value, in addition our $T_{\rm eff} = 5480 \pm 66$ ($>3\sigma$) and $\log(g) = 4.80 \pm 0.33$ (within 1σ). We find our Mg/Si value to be 0.96 ± 0.18 and C/O to be 0.41. The Mg/Si ratio is within 1σ of the literature value, but our derived C/O ratio is $>3\sigma$ from the literature value.

Previous abundance measurements for BD +60 1417 (K0) use iSpec (S. Blanco-Cuaresma 2019; C. L. Phillips et al. 2024) and report a substellar $\mathrm{C/O} = 0.23 \pm 0.12$ and enhanced Mg/Si $= 1.41 \pm 0.19$. Compared to C. L. Phillips et al. (2024), we find a C/O of 0.33 ± 0.07 compared to 0.23 ± 0.12 (within 1σ). Contrarily, we do not report an enhanced Mg/Si ratio 0.84 ± 0.14 versus 1.41 ± 0.19. We investigate whether our abundance discrepancy is due to different choices of solar normalization of M. Asplund et al. (2009, hereafter ASP2009) versus N. Grevesse et al. (2007, hereafter GR2007). We determine our abundances using ASP2009 and GR2007 solar abundances values. We find that our determined abundances are within 1σ of each other from the two different normalizations. Thus, we rule out discrepancy due to solar normalization choices.

5. Discussion

With our parameters and abundances in hand, we can investigate a number of aspects of the benchmark brown dwarf systems. In this section, we discuss the implications of our results.

5.1. Metallicity

The comparison between the metallicity of brown dwarfs and that of their host stars provides a powerful diagnostic of formation pathways (B. Ma & J. Ge 2014; A. D. Adams et al. 2023; Z. Zhang et al. 2023; J. W. Xuan et al. 2024a; W. W. Meynardie et al. 2025). If a brown dwarf forms through the starlike route of gravitational collapse and fragmentation of a molecular cloud, it should share the same [Fe/H] as its host star, reflecting a common origin in the same natal environment (K. Hawkins et al. 2020; C.-C. Hsu et al. 2024; A. Sinha et al. 2026). This expectation contrasts with the formation of planets, which exhibit a strong dependence on host star metallicity. It is now well established that giant planets are more commonly found orbiting metal-rich stars, known as the planet metallicity correlation (D. A. Fischer & J. Valenti 2005). From observational studies, brown dwarf–metallicity correlation is not as strongly correlated as planet metallicity, where stellar hosts of giant planets are more metal rich. In contrast, stars that host brown dwarfs have compositions resembling those of stars with low-mass planets; α-elements ($[X_\alpha/\mathrm{Fe}]$, which include Mg, Si, Ca, and Ti), and iron-peak elements ($[X_{\rm Fe}/\mathrm{Fe}]$, which include Cr, Mn, Co, and Ni) appear solar, compared to the $\sim$+0.15 dex peak in giant-planet hosts (D. A. Fischer & J. Valenti 2005; J. Sahlmann et al. 2011; B. Ma & J. Ge 2014; D. Mata Sánchez et al. 2014; J. Maldonado & E. Villaver 2017). Taken together, these results indicate the absence of a statistically significant metallicity correlation for brown dwarf host stars.

For most of our stars, we find a near-solar metallicity. However, compared to the current population of host stars of directly imaged planets (A. Baburaj et al. 2025, 2026), our spread in [Fe/H] for wider-orbit brown dwarfs is larger (Figure 6). The larger spread is in part due to a number of stars that are metal-poor: HIP 63506 (K6), LP 617-58 (G8), NLTT 1011 (K7), and BD +06 2986 (K8). In metal-poor stars, fewer heavy elements lead to weaker absorption features, making abundance determination difficult. For our metal-poor stars we see this effect for a number of lines, including O I, Ca I, and Si I, as demonstrated in Figure 7. For a number of these metal-poor stars, we note enhanced Mg/Si ratios; in particular, NLTT 1011 and BD +06 2986, with Mg/Si $= 2.47 \pm 0.20$ and 1.47 ± 0.29, respectively, have silicon depletion, [Si/H] $= -0.77$ (upper limit) and -0.72 ± 0.10, respectively.

To investigate the validity of our finding that some of our stars are metal-poor, we examined previous measurements in the literature for both the host star and its companion. The companion T dwarf, ULAS J150457.65+053800.8, to BD +06 2986 is classified as a metallicity benchmark subdwarf with [M/H] $= -0.47^{+0.09}_{-0.10}$ (Z. H. Zhang et al. 2019; A. J. Burgasser et al. 2025). We find a host star metallicity ([Fe/H] $= -0.82 \pm 0.15$), along with previous literature measurements that support a subsolar metallicity environment. From the MILES survey, A. E. García Pérez et al. (2021) and P. Prugniel et al. (2011) find an [Fe/H] $= -1.32 \pm 0.0$ and -0.83 ± 0.15, respectively. Previous works find an [Fe/H] ≈ -0.38, which is closer to the metallicity for the brown dwarf companion and supports a metal-poor environment (A. Arentsen et al. 2019). We report a subsolar metallicity for LP 617-58 of [Fe/H] $= -0.39 \pm 0.01$, which is in line with the spectroscopic literature value reported of [Fe/H] $= -0.36 \pm 0.04$ (M. Xiang et al. 2019) from low-resolution ($R\sim1800$) spectra from LAMOST DR5. The photometric [Fe/H] from Gaia DR3 for LP 617-58 is subsolar, -0.23 ± 0.01. Two of our other metal-poor stars, NLTT 1011 and HIP 63506, do not have reported literature measurements for comparison.

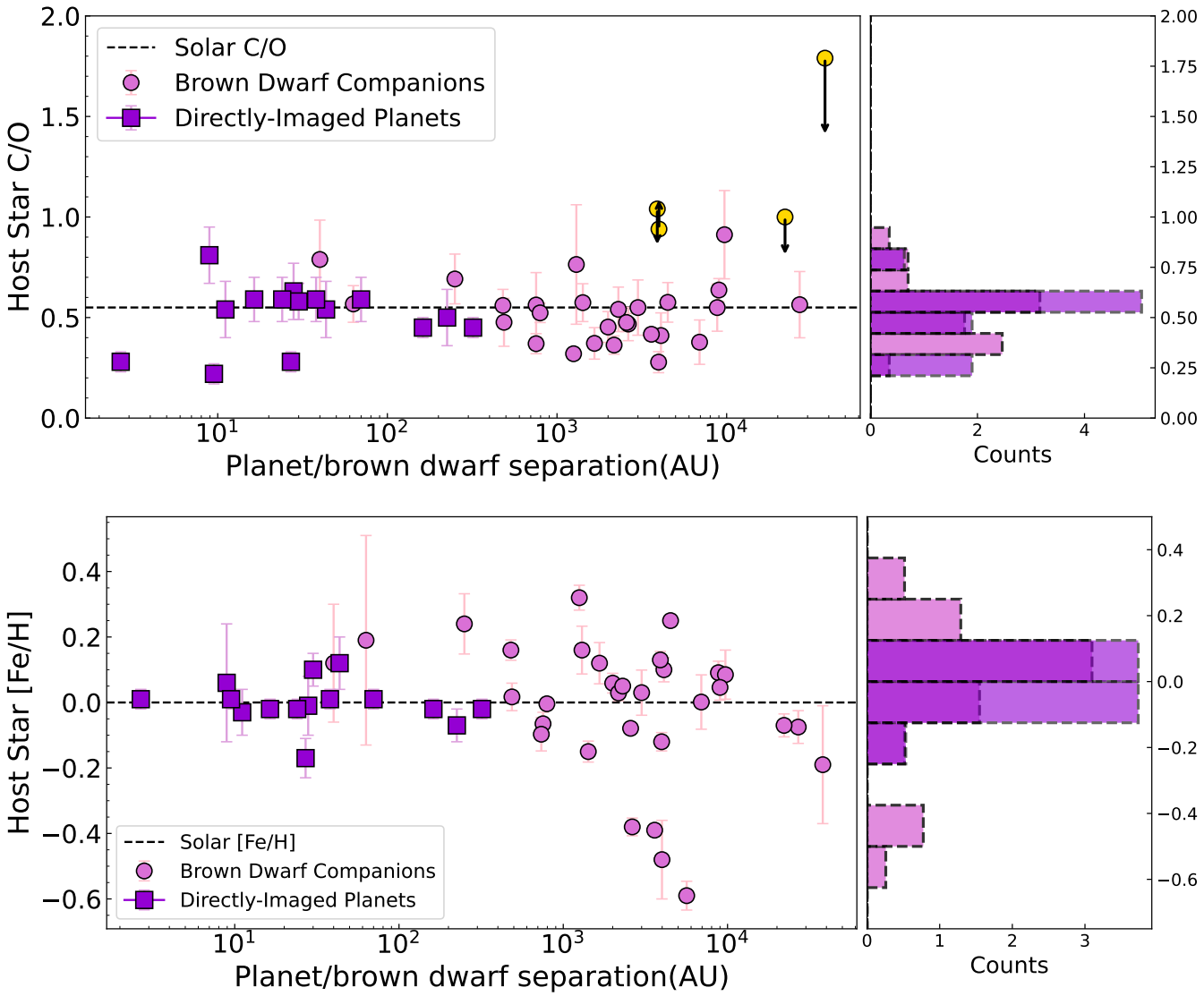


Figure 6. Top: host star C/O ratios for directly imaged planets (purple squares) vs. brown dwarf companions (pink circles) in this sample with FGK hosts. Host stars of brown dwarf companions that only have an upper limit on the C/O ratio are shown with gold circles. The dashed black line indicates the solar C/O ratio. Bottom: host star metallicity ([Fe/H]) ratios for directly imaged planets (purple squares) vs. brown dwarf companions (pink circles) in this sample with FGK hosts. The dashed black line indicates the solar metallicity ratio. Directly imaged planets are a compilation from A. Baburaj et al. (2025, 2026).

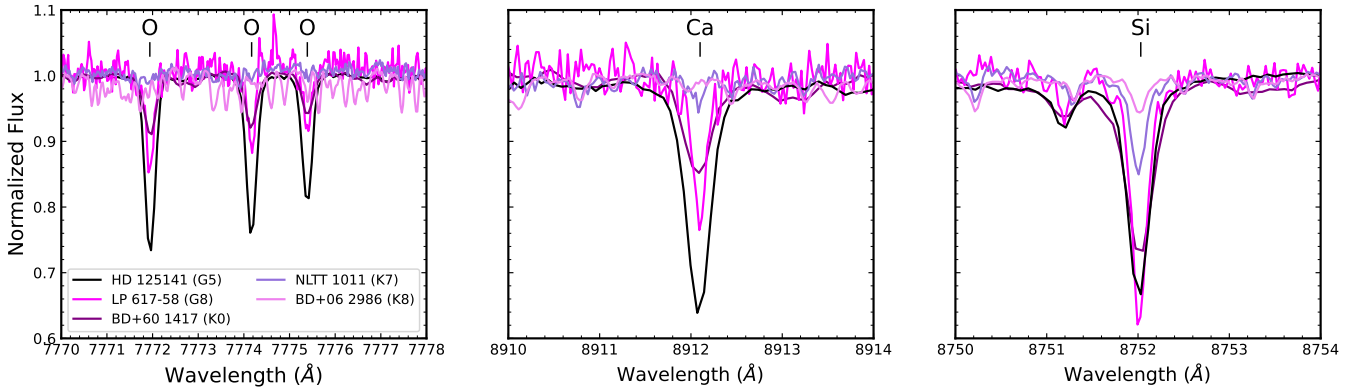


Figure 7. PEPSI spectra of stars of different spectral types, HD 125141 (G5), LP 617-58 (G8), BD +60 1417 (K0), NLTT 1011 (K7), and BD +06 2986 (K8), in selected wavelength regions of 7770–7778 Å (left), 8910–8914 Å (middle), and 8750–8754 Å (right). Line features used in the abundance analysis have been labeled.

5.2. Silicate Cloud Prediction from Host Star Chemistry

As brown dwarfs cool and evolve from spectral classes M to Y, they experience dynamic changes in the atmospheric properties and subsequent cloud formation. L dwarfs have a typical temperature regime of ∼1300–2200 K, which favors the formation of atmospheric condensates (F. Allard et al.

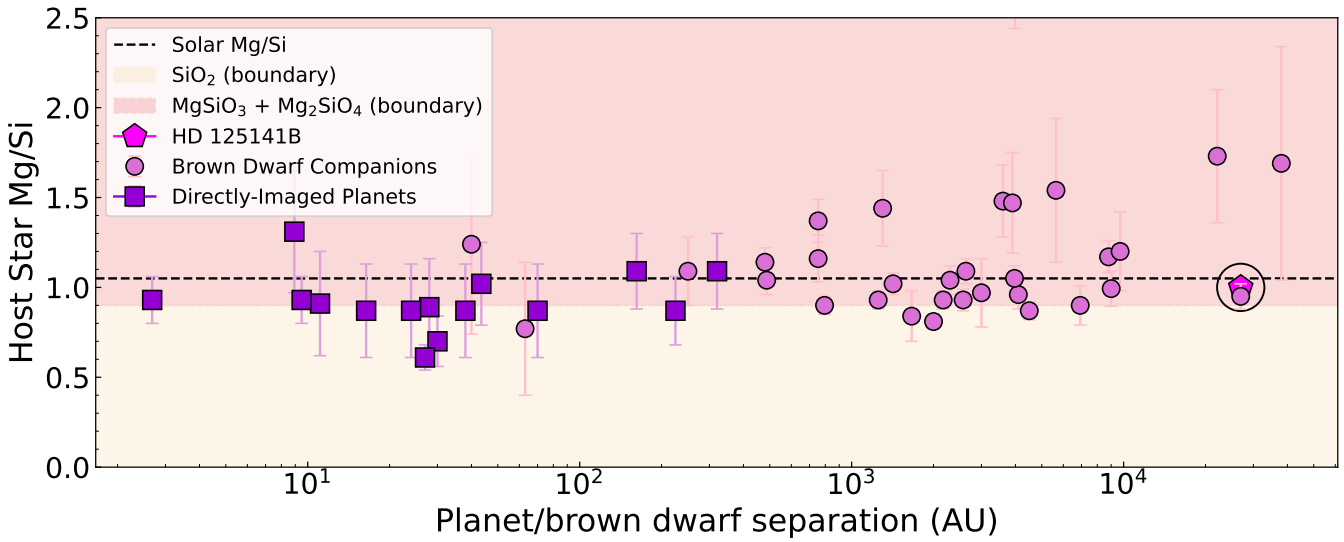


Figure 8. Host star Mg/Si ratios for directly imaged planets (purple squares) and brown dwarf companions in this sample with FGK hosts. The dashed line represents solar Mg/Si ratio. We denote the region for SiO_2 cloud predictions and $Mg_2SiO_4 + MgSiO_3$ from E. Calamari et al. (2024). We highlight recent retrieval results from V. Kecskeméthy et al. (2026, in preparation) that demonstrates the similarities between host star Mg/Si and inferred Mg/Si of the brown dwarf companion to HD 125141.

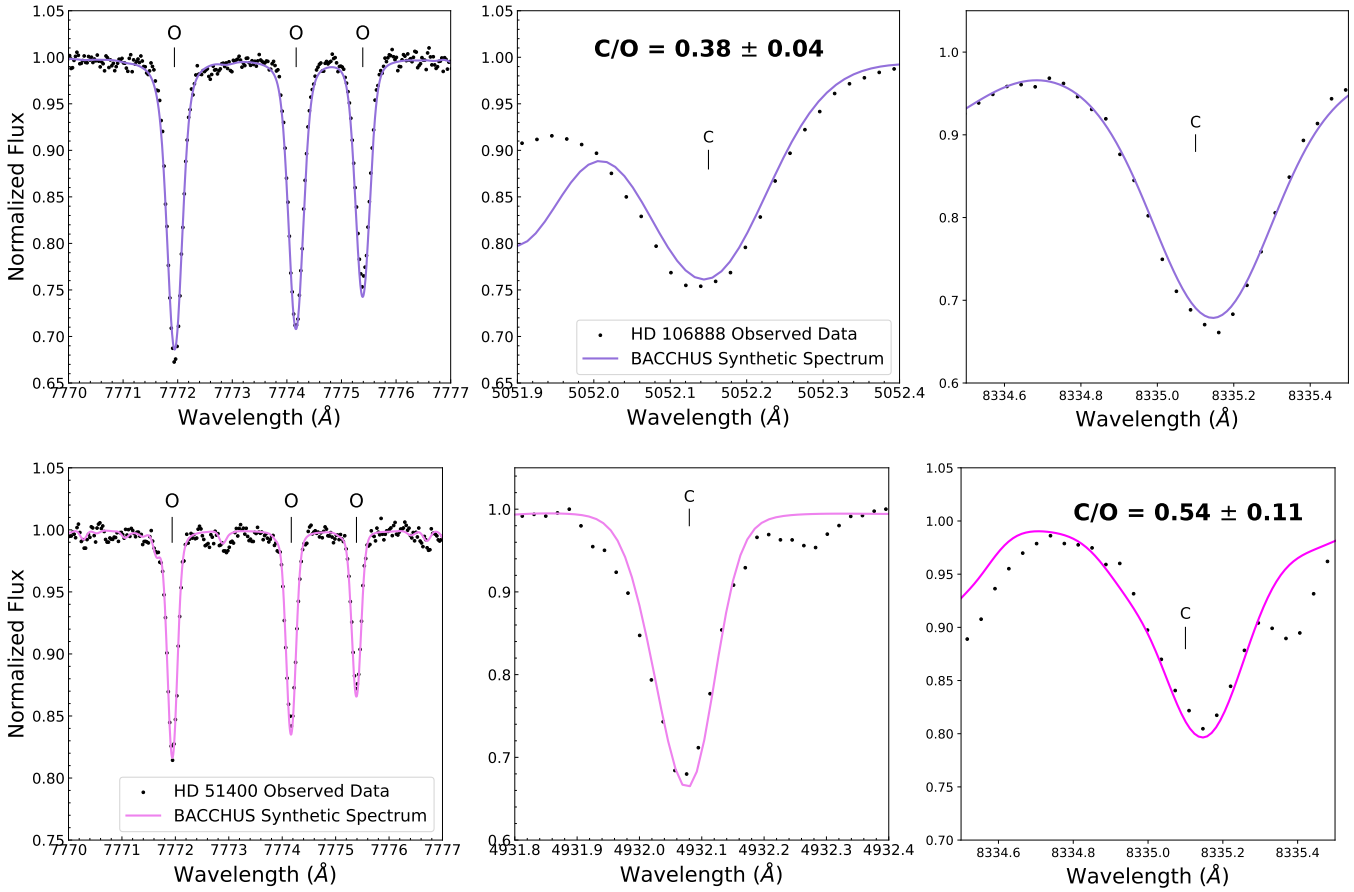


Figure 9. Top: the O I triplet line and two different carbon lines used to calculate the C/O ratio for HD 106888, which yields a subsolar C/O ratio and smaller error bars. Bottom: O I triplet line and two different carbon lines used to calculate the C/O ratio for HD 514000, which yields a near-solar C/O ratio and larger error bars.

2001). These clouds are primarily composed of silicate species such as enstatite, forsterite, quartz, and SiO, along with aluminum oxides, like corundum, and Fe in the lower layers.

Both Ca and Al are highly refractory elements that condense into solid grains at high temperatures, primarily as Al_2O_3 (corundum) and $CaTiO_3$ (perovskite) (Lewis 2004; H. R. Wakeford et al. 2016). Although their overall abundances are lower than more dominant refractories such as Mg, Si, and Fe, the relative abundance of Ca to Al can influence which condensates dominate at a given condensation

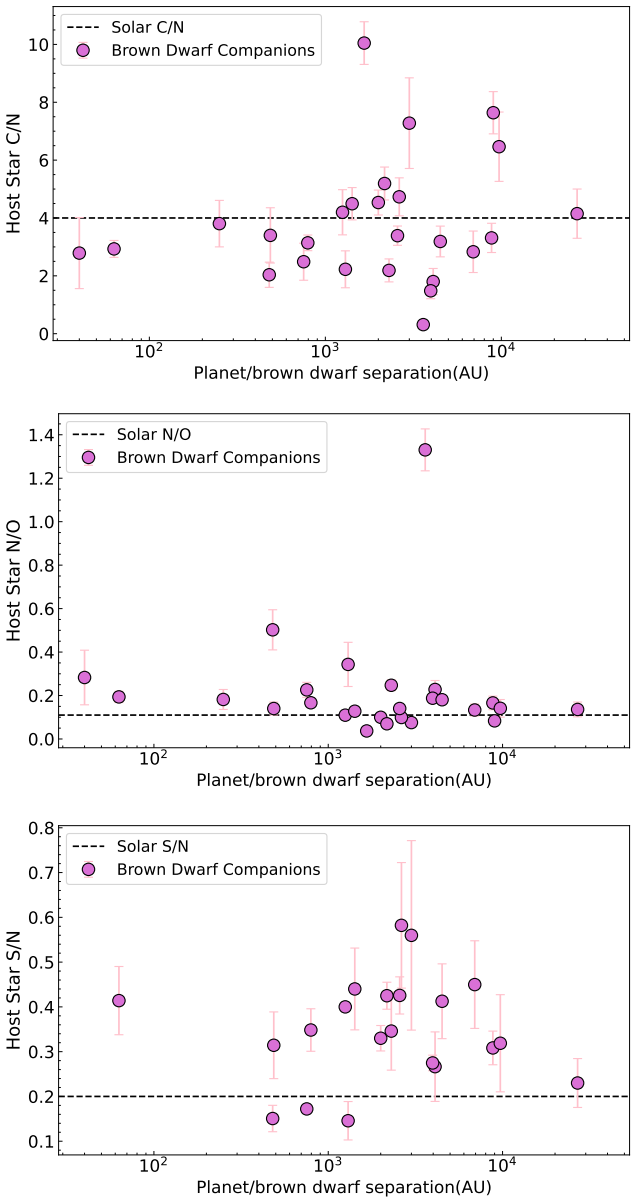


Figure 10. Top: host star C/N vs. separation for our sample. Middle: host star N/O vs. separation. Bottom: S/N vs. separation.

temperature. A lower Ca/Al ratio favors Al-bearing condensates such as corundum, which act as efficient cloud seeds and can lead to thicker, more optically dense cloud decks (F. Allard et al. 2001; C. Helling et al. 2008). In contrast, a higher Ca/Al ratio promotes the early formation of Ca-bearing species such as perovskite and $Ca_2Al_2SiO_7$ (gehlenite), which accelerate the depletion of Ti from the gas phase and thus influence the disappearance of TiO and VO bands during the spectral transition from M to L dwarfs (K. Lodders 2002; C. Helling et al. 2008; P. Woitke et al. 2020). While condensation temperature primarily determines the sequence in which species solidify, variations in Ca/Al ratios provide context for modeling early cloud formation, cloud opacity, and spectral diversity in brown dwarf atmospheres.

From the theoretical chemical framework presented in E. Calamari et al. (2024), we can predict cloud species of brown dwarfs based on FGK host star chemical abundances for well-known silicates enstatite ($MgSiO_3$), forsterite (Mg_2SiO_4) and quartz (SiO_2). The relative Mg/Si abundance ratio and prediction of cloud species are as follows:

1. Mg/Si $\lesssim$ 0.9: enstatite + quartz;
2. Mg/Si $\sim$ 0.9: enstatite;
3. Mg/Si $\gtrsim$ 0.9: enstatite + forsterite.

We use the chemical network from E. Calamari et al. (2024) to predict the formation of cloud species of our sample (Table 9). Generally, we find that our Mg/Si ratios are roughly solar (1.05; N. Grevesse et al. 2007; M. Asplund et al. 2009) or higher. This would result in the production of mainly enstatite and forsterite clouds for our sample. There are, however, a number of systems with Mg/Si that predict SiO_2 or quartz clouds. Future retrieval analyses could provide deeper insight into the potential presence of SiO_2 and contribute to the expanding catalog of substellar objects exhibiting SiO_2 clouds (B. Burningham et al. 2021).

We compare the host star Mg/Si ratios for current wide-orbit directly imaged planet host stars and our sample of host stars of brown dwarfs in Figure 8. We find that the median Mg/Si ratio for our host star sample is $\approx$1.04, indicating the primary prediction that enstatite and forsterite clouds might form in the companion. We find that the average Mg/Si for the directly imaged planets host stars is $\approx$0.89, which predicts enstatite + quartz cloud formation.

5.2.1. Testing Host Brown Dwarf Companion Mg/Si Connections

In this work, we adopt the hypothesis that brown dwarf companions broadly reflect the elemental abundance patterns of their host stars, as predicted by phase equilibrium condensation models (K. Lodders 2002, 2003; M. S. Marley et al. 2002). However, this assumption remains largely untested. The advent of JWST enables detailed atmospheric retrievals that can constrain cloud composition and refractory element ratios (e.g., K. K. W. Hoch et al. 2025; Z. Zhang et al. 2025b). Recent works have begun to explore the question of whether brown dwarf and giant exoplanets inherit their host star Mg/Si chemistry (E. Calamari et al. 2024; E. Calamari et al. 2026). Establishing observational constraints on refractory ratios in substellar atmospheres is therefore a critical step toward testing this phase equilibrium connection. B. Burningham et al. (2021) used the column density (N) retrieved from the magnesium- and oxygen-bearing cloud species to infer Mg/Si ratios of a brown dwarf companion. Using the *Brewster* framework (B. Burningham et al. 2021), V. Kecskeméthy et al. (2026, in preparation) recently found that the companion to HD 125141 has an inferred Mg/Si ratio of 1.00, which is in close proximity to our determined Mg/Si ratio of 0.95 $\pm$ 0.07, which suggests chemical similarities between the host and the brown dwarf companion. A total of 14/32 of our host star sample have current or incoming JWST NIRSpec/PRISM and MIRI/LRS data for the brown dwarf companion, which will enable detailed studies of silicate-based cloud properties. Future retrieval analysis with extended wavelength coverage enabled by JWST will allow for tests of whether these brown dwarf systems show similar Mg/Si chemical composition to their host stars, as recently found with an ultrahot Jupiter (J. A. Sanchez et al. 2026).

Table 8
Key Abundance Ratios and Errors for the PEPSI Sample

Object	C/O	Mg/Si	Ca/Al	[Y/Mg]	S/N
HD 89744	0.56 ± 0.09	0.77 ± 0.37	0.72 ± 0.06	−0.02 ± 0.44	0.41 ± 0.07
HD 46588	0.57 ± 0.09	1.02 ± 0.06	0.77 ± 0.06	0.00 ± 0.14	0.44 ± 0.09
*54 Psc	0.56 ± 0.08	1.14 ± 0.08	0.69 ± 0.05	−0.16 ± 0.09	0.15 ± 0.02
V* HN Peg	0.52 ± 0.04	0.90 ± 0.05	1.29 ± 0.09	0.11 ± 0.07	0.34 ± 0.04
HD 126053	0.46 ± 0.08	1.09 ± 0.07	0.69 ± 0.05	−0.19 ± 0.18	0.58 ± 0.14
GJ 417	0.45 ± 0.07	0.81 ± 0.04	0.94 ± 0.08	0.12 ± 0.13	0.32 ± 0.02
HIP 9269	0.76 ± 0.29	1.44 ± 0.21	0.52 ± 0.11	−0.26 ± 0.18	0.14 ± 0.04
G171-58	0.54 ± 0.11	1.17 ± 0.09	0.89 ± 0.13	−0.11 ± 0.12	0.30 ± 0.03
HIP 26653 (HD 37216)	0.56 ± 0.16	1.37 ± 0.12	0.77 ± 0.07	−0.06 ± 0.13	0.17 ± 0.03
HD 106888	0.38 ± 0.04	0.93 ± 0.05	0.74 ± 0.08	0.13 ± 0.10	0.42 ± 0.03
HD 51400	0.54 ± 0.11	1.04 ± 0.08	0.80 ± 0.08	0.04 ± 0.10	0.34 ± 0.08
HD 203030	0.47 ± 0.11	1.04 ± 0.08	1.03 ± 0.07	0.09 ± 0.16	0.31 ± 0.07
HD 8291	0.47 ± 0.04	0.93 ± 0.06	1.06 ± 0.11	0.15 ± 0.06	0.42 ± 0.04
HD 16270	0.69 ± 0.12	1.09 ± 0.19	0.66 ± 0.14	0.01 ± 0.20	⋯
HD 116012	0.91 ± 0.21	1.20 ± 0.22	0.57 ± 0.8	<−0.94	0.31 ± 0.10
BD +21 55	0.27 ± 0.05	1.05 ± 0.07	0.71 ± 0.07	−0.10 ± 0.75	0.27 ± 0.01
BD +60 1417	0.37 ± 0.07	0.84 ± 0.14	0.93 ± 0.13	0.14 ± 0.26	⋯
StKM 2-1777	<1.00	1.73 ± 0.37	0.21 ± 0.05	−0.06 ± 0.03	⋯
HD 253662	0.32 ± 0.01	0.93 ± 0.05	0.89 ± 0.09	0.08 ± 0.03	0.40 ± 0.01
CD –24 407	0.37 ± 0.11	0.90 ± 0.11	0.79 ± 0.10	−0.08 ± 0.22	0.44 ± 0.09
BD +13 2269	0.41 ± 0.11	0.96 ± 0.08	1.10 ± 0.12	0.11 ± 0.16	0.26 ± 0.07
BD +01 299	0.78 ± 0.19	1.24 ± 0.5	0.73 ± 0.22	0.01 ± 0.31	⋯
StKM 1-1526	< 1.04	1.47 ± 0.28	1.04 ± 0.11	−0.06 ± 0.03	⋯
TYC 5213-545-1	0.63 ± 0.05	0.99 ± 0.09	0.90 ± 0.13	0.01 ± 0.11	⋯
LP 617-58	0.41 ± 0.03	1.48 ± 0.20	0.56 ± 0.11	−0.42 ± 0.07	⋯
HIP 63506	⋯	1.54 ± 0.40	1.59 ± 0.34	<−0.54	⋯
LSPM J0632+5053	0.57 ± 0.09	0.87 ± 0.05	0.83 ± 0.08	0.14 ± 0.10	0.41 ± 0.08
NLTT 1011	>0.94	2.64 ± 0.20	<−0.88	<−0.314	⋯
HD 125141 (G200-28)	0.56 ± 0.16	0.95 ± 0.07	0.76 ± 0.09	−0.11 ± 0.23	0.22 ± 0.05
BD +06 2986	⋯	1.47 ± 0.29	2.70 ± 0.50	<−0.687	⋯
BD +24 4329	<1.79	1.69 ± 0.65	<1.37	−0.08 ± 0.42	⋯
BD +49 2561	0.54 ± 0.13	0.97 ± 0.19	0.77 ± 0.09	0.04 ± 0.19	0.55 ± 0.21

5.3. C/O Ratio: Formation and Oxygen Sinks

The carbon-to-oxygen (C/O) ratio is widely considered a key diagnostic of substellar formation pathways (K. I. Öberg et al. 2011, 2023). Comparison of the C/O ratio of a brown dwarf to that of its host star can offer valuable insight into the origin of the companion (J. Wang et al. 2022; J. W. Xuan et al. 2022; A. D. Adams et al. 2023; W. W. Meynardie et al. 2025). If the brown dwarf formed via gravitational collapse of a molecular cloud or through gravitational instabilities within a protoplanetary disk, processes that involve well-mixed material, its C/O ratio is expected to resemble that of the host star (M. R. Bate et al. 2002; M. W. Phillips et al. 2024; A. A. Ahmad et al. 2025; N. Vowell et al. 2025). Similarly, a stellar-like C/O ratio is anticipated for planets that form inside the snowline of both water and carbon grains. In contrast, a superstellar C/O ratio may suggest that the companion's atmosphere formed primarily from gas accreted beyond the water snowline, consistent with core-accretion scenarios. The formation location and possible migration history of the companion can be inferred by comparing its current position to the ice lines of key molecules such as water (H_2O), carbon dioxide (CO_2), and carbon monoxide (CO) in the protoplanetary disk (K. I. Öberg et al. 2011, 2023).

Potential trends with the C/O ratio have been investigated in the literature, and at least for directly imaged planets, the C/O ratio appears consistently near solar, and potential trends between C/O and separation have been identified (K. K. W. Hoch et al. 2023). Recent work has focused on the C/O ratio of brown dwarf companions, and current trends suggest near-solar composition (J. C. Costes et al. 2024; C.-C. Hsu et al. 2024; J. W. Xuan et al. 2024a; J. Kammerer et al. 2025). While some brown dwarfs have been found to have supersolar C/O ratios (E. Calamari et al. 2022; J. Gaarn et al. 2023), these have recently been rectified with the discoveries of binarity for Gl 229B (Gl 229Ba and Gl 229Bb) and updated line lists for analysis of Ross 458 c with JWST/NIRSpec (J. W. Xuan et al. 2024b; W. W. Meynardie et al. 2025).

Historically, forward modeling and atmospheric retrieval analyses of brown dwarf companions have often assumed a solar C/O ratio, implicitly treating host stars as chemically homogeneous and representative of the solar neighborhood (J. W. Xuan et al. 2024a). This assumption is particularly common for wide-separation brown dwarfs, where stellar-like formation pathways such as turbulent fragmentation or gravitational instability are expected to produce companions that inherit the elemental composition of their host stars (A. P. Boss 1997; A. G. W. Cameron 1978). Recent efforts have established that there is a diversity of C/O ratios between directly imaged companion hosts (A. Baburaj et al. 2025, 2026). Our determined host star C/O ratios shown in Figure 6 demonstrate that the stellar environments in which brown dwarfs form exhibit similar chemical diversity. We implement the Anderson–Darling (AD) test to determine whether the C/O and [Fe/H] distributions of directly imaged planet host stars and our PEPSI sample of brown dwarf host stars are statistically different. For the C/O ratios, we find an AD statistic $= -0.01$ and p-value of 0.25. This indicates that

Table 9
Prediction of Cloud Species to Form in Brown Dwarf Companion from Mg/Si Ratio of Host Star

Object	Mg/Si	Cloud Species Predicted
*54 Psc	1.14	Enstatite + forsterite
BD +01 299	1.24	Enstatite + forsterite
BD +13 2269	0.96	Enstatite + forsterite
BD +49 2561	0.97	Enstatite + forsterite
BD +60 1417[a]	0.84	Enstatite + quartz
BD +21 55	1.05	Enstatite + forsterite
CD –24 407	0.90	Enstatite
G171-58	1.17	Enstatite + forsterite
GJ 417[a]	0.81	Enstatite + quartz
HD 106888	0.93	Enstatite + forsterite
HD 116012	1.20	Enstatite + forsterite
HD 125141	0.95	Enstatite + forsterite
HD 126053	1.09	Enstatite + forsterite
HD 16270	1.09	Enstatite + forsterite
HD 203030[a]	1.04	Enstatite + forsterite
HD 253662[a]	0.93	Enstatite + forsterite
HD 46588[b]	1.02	Enstatite + forsterite
HD 51400	1.04	Enstatite + forsterite
HD 8291	0.93	Enstatite + forsterite
HD 89744[b]	0.77	Enstatite + quartz
HIP 26653[b]	1.37	Enstatite + forsterite
HIP 63506	1.54	Enstatite + forsterite
V* HN Peg[b]	0.90	Enstatite
HIP 9269	1.44	Enstatite + forsterite
StKM 2-1777	1.73	Enstatite + forsterite
StKM 1-1526	1.47	Enstatite + forsterite
TYC 5213-545-1	0.99	Enstatite + forsterite
LP 617-58	1.48	Enstatite + forsterite
LSPM J0632+5053	0.87	Enstatite + quartz
NLTT 1011[b]	2.64	Enstatite + forsterite
BD +06 2986	1.47	Enstatite + forsterite
BD +24 4329	1.69	Enstatite + forsterite
BD +49 2561	0.97	Enstatite + forsterite

Notes.
[a] These targets are observed and/or scheduled to be observed as a part of JWST programs with NIRSpec and/or MIRI instruments (GO #8140).
[b] These targets are observed and/or scheduled to be observed as a part of JWST programs with NIRSpec and/or MIRI instruments (GO #3670).

Table 10
Estimation of Percentage of Oxygen Lost from Silicate-based Clouds Based on Host Star Chemistry

Object	Oxygen Sink Percentage
*54 Psc	25.2% ± 4.7%
BD +01 299	26.0% ± 16.5%
BD +13 2269	26.9% ± 9.7%
BD +49 2561	22.7% ± 12.1%
BD +60 1417	13.6% ± 6.9%
BD +21 55	17.7% ± 2.7%
CD –24 407	20.2% ± 9.1%
G171-58	13.5% ± 5.4 %
GJ 417	16.3% ± 5.4%
HD 106888	8.8% ± 1.6%
HD 116012	33.1% ± 19.2%
HD 125141	20.5% ± 11.0%
HD 126053	20.7% ± 6.0%
HD 16270	21.8% ± 9.5%
HD 203030	25.5% ± 7.5%
HD 253662	17.8% ± 2.2%
HD 46588	16.4% ± 5.1%
HD 51400	26.7% ± 6.6%
HD 8291	18.5% ± 2.4%
HD 89744	16.7% ± 8.4%
HIP 26653	26.5% ± 9.1%
HIP 63506	25.0% ± 11.9 %
V* HN Peg	19.6% ± 2.3%
HIP 9269	31.3% ± 20.1%
StKM 2-1777	25.2% ± 9.6%
StKM 1-1526	…
TYC 5213-545-1	21.0% ± 4.3%
LP 617-58	21.7% ± 2.5%
LSPM J0632+5053	25.7% ± 4.3%
NLTT 1011	…
BD +06 2986	…
BD +24 4329	…
BD +49 2561	22.7% ± 12.0%

the two populations are similar, but with low confidence. For the [Fe/H] abundances, we find an AD statistic = 1.41 with a p-value = 0.08; this remains slightly above the standard p-value = 0.05 significance threshold.

As our C/O ratios have a range of precision from 0.03 to 0.29 for solar and subsolar C/O ratios, we examine the BACCHUS fits. We compare the subsolar C/O BACCHUS fits for HD 106888 and near-solar C/O fits for HD 51400, with 0.04 and 0.11 error on the C/O, respectively (Figure 9). Both targets have similar precision for $T_{\rm eff}$, $\log(g)$, and [Fe/H], but HD 51400 has higher errors for [C/H] and [O/H], resulting in a higher propagated error in its C/O ratio.

5.3.1. Oxygen Sink Fraction

Discrepancies between atmospheric and host star C/O do not uniquely diagnose formation pathways and must be interpreted in the context of atmospheric chemistry and cloud physics. Condensation of oxygen-bearing species such as H_2O, silicates, and other metal oxides, followed by rainout, can remove oxygen from the observable atmosphere of a brown dwarf, yielding elevated C/O ratios even when the bulk composition matches that of the host star.

We use the formulae from E. Calamari et al. (2024) to determine the relative percentage of oxygen lost in the brown dwarf companion from the host star oxygen budget:

$$\Sigma O_{\rm cloud} = 2\Sigma Si + \Sigma Mg + \Sigma Ca + 1.5\Sigma Al + 2\Sigma Ti + \Sigma V \quad (5)$$

$$O_{\rm sink} = \frac{\Sigma O_{\rm cloud}}{\Sigma O}. \quad (6)$$

We convert metallicity measurements expressed in logarithmic (dex) notation to absolute molar abundances relative to hydrogen following N. R. Hinkel et al. (2022).

E. Calamari et al. (2024) found that, from compositional benchmarks in comparison to the local solar neighborhood population from J. M. Brewer et al. (2016), the median oxygen sink is $17.8^{+1.7}_{-2.3}$%. We find that on average our oxygen sink percentage lies at the higher end of the local neighborhood (21.40% ± 5.39%; Table 10). In future modeling via retrievals or forward modeling, we would expect this to have implications on the retrieved versus bulk C/O ratio (e.g., V. Kecskeméthy et al. 2026, in preparation).

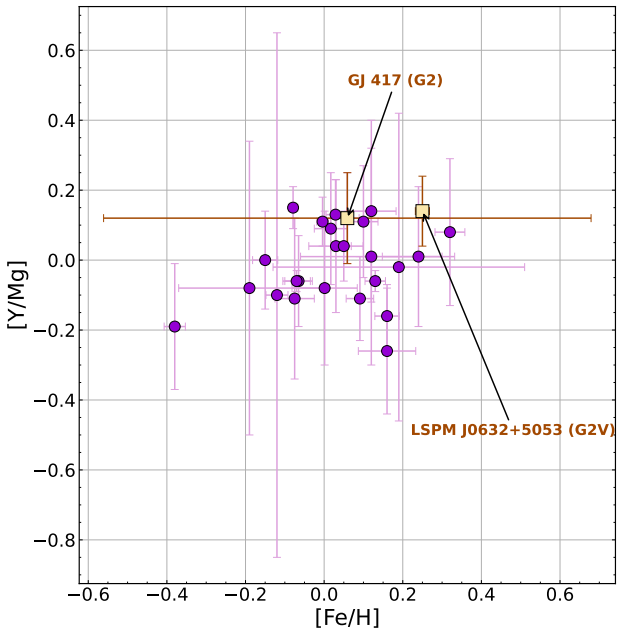


Figure 11. [Y/Mg] vs. [Fe/H] (metallicity) for our sample of FGK stars (purple circles). We highlight solar twins (G2)−GJ 417 and LSPM J0632 +5053 in yellow squares.

5.4. Formation and Migration Tracers

Elemental abundance ratios (such as C/O, N/O, C/N, and S/N) in protoplanetary disks serve as powerful tracers of formation and migration histories (D. Turrini et al. 2021). By comparing the atmospheric abundances of a substellar companion to its host star, shown as

$$X/Y^{*} = \frac{(X_{\rm comp}/Y_{\rm comp})}{(X_{\rm star}/Y_{\rm star})} \quad (7)$$

following J. R. Kolecki & J. Wang (2022), multielemental analysis can break degeneracies between starlike cloud collapse and disk-born formation pathways (Figure 10 and Table 11).

While we do not currently possess the precise atmospheric abundance measurements for this brown dwarf sample to calculate these companion-to-star ratios, future high-SNR observations, particularly with JWST, will enable these multielemental constraints by targeting key nitrogen- and sulfur-bearing species.

Measuring nitrogen in brown dwarfs remains challenging because N_2 is spectroscopically inactive. Instead, the primary tracers are NH_3 in T dwarfs, HCN in warmer objects, and potentially NH (imidogen) (A. N. Perri & L. K. McKemmish 2024), though NH also serves as a theoretical temperature diagnostic in equilibrium chemistry (K. Lodders 2002). Future or current JWST observations of later-type T dwarf companions can reveal NH_3 features in the mid-infrared, significantly improving constraints on the total nitrogen budget and allowing for accurate determinations of C/N and N/O ratios.

Complementarily, sulfur species play a key role in shaping the atmospheric chemistry and cloud structures of cooler brown dwarfs. In some of the T dwarfs in our sample, H_2S is anticipated to be the dominant molecular carrier across a broad range of temperatures, eventually condensing into MnS, Na_2S, ZnS, and NH_2SH cloud layers (C. Visscher et al. 2006; C. V. Morley et al. 2012). JWST's access to these mid-infrared molecular features (W. W. Meynardie et al. 2025) can provide the full suite of volatile abundances required to directly test these formation frameworks and illuminate the evolutionary histories of these brown dwarf systems.

Table 11
Abundance Ratios and Errors for the PEPSI Sample Related to Additional Formation and Migration Diagnostics from D. Turrini et al. (2021)

Object	N/O	C/N
HD 89744	0.19 ± 0.02	2.94 ± 0.29
HD 46588	0.12 ± 0.01	4.49 ± 0.55
*54 Psc	0.50 ± 0.09	2.03 ± 0.43
V* HN Peg	0.16 ± 0.01	3.14 ± 0.27
HD 126053	0.09 ± 0.01	4.74 ± 0.65
GJ 417	0.09 ± 0.01	4.53 ± 0.43
HIP 9269	0.34 ± 0.10	2.22 ± 0.63
G 171-58	0.16 ± 0.03	3.31 ± 0.50
HIP 26653	0.22 ± 0.03	2.48 ± 0.63
HD 106888	0.06 ± 0.01	5.19 ± 0.56
HD 51400	0.24 ± 0.02	2.18 ± 0.39
HD 203030	0.14 ± 0.02	3.39 ± 0.95
HD 8291	0.14 ± 0.01	3.38 ± 0.33
HD 16270	0.18 ± 0.04	3.80 ± 0.80
HD 116012	0.14 ± 0.04	6.46 ± 1.19
BD +21 55	0.18 ± 0.01	1.48 ± 0.27
BD +60 1417	0.03 ± 0.01	10.04 ± 0.73
SkTKM 2-1777	…	…
HD 253662	0.10 ± 0.01	2.95 ± 0.14
CD −24 407	0.13 ± 0.02	2.83 ± 0.71
BD +13 2269	0.22 ± 0.04	1.80 ± 0.45
BD +01 299	0.28 ± 0.12	2.78 ± 1.22
StKM 1-1526	…	…
TYC 5213-545-1	0.08 ± 0.01	7.63 ± 0.72
LP 617-58	1.33 ± 0.09	0.31 ± 0.02
HIP 63506	…	…
LSPM J0632+5053	0.18 ± 0.01	3.18 ± 0.53
NLTT 1011	…	…
HD 125141	0.13 ± 0.03	4.14 ± 0.85
BD +06 2986	…	…
BD +24 4329	…	…
BD +49 2561	0.07 ± 0.01	7.27 ± 1.56

6. Ages from Y/Mg

As brown dwarfs contract and cool over time, their apparent properties depend strongly on both mass and age. Without an independent age estimate, disentangling these parameters is fundamentally degenerate (A. Burrows et al. 2001, 2011; I. Baraffe et al. 2002, 2015). Observable quantities such as luminosity and effective temperature are sensitive to both age and mass, producing a well-known degeneracy among these parameters. Several approaches can help break this degeneracy, including membership in clusters or young moving groups, kinematic analyses, spectroscopic gravity indicators, the lithium test, or association with binary or multiple-star systems (J. D. Kirkpatrick et al. 2008; K. M. Aller et al. 2016; C. L. Phillips et al. 2020; J. Gagné et al. 2023). In particular, binary or comoving systems provide a unique opportunity: if the primary companion star can be characterized in detail, its properties can yield valuable age constraints for all components of the system.

Recent studies have proposed the abundance ratio [Y/Mg] as a useful diagnostic of stellar age for solar-type stars (P. E. Nissen 2015; M. Tucci Maia et al. 2016; O. J. Katime Santrich et al. 2022; B. Ratcliffe et al. 2024;

Table 12
Comparison of Stellar Ages: Literature versus [Y/Mg]-based Estimates

Object	Previous Age (Gyr)[a]	[Y/Mg] (Gyr)	Age Estimate Method	References
HD 89744[b]	1.5–3	6.19 ± 19.42	Isochrone fitting	J. C. Wilson et al. (2001)
HD 46588	1.3– 4.3	5.44 ± 6.43	Isochrone fitting	L. Casagrande et al. (2011)
*54 Psc	0.7–4.7	12.55 ± 4.90	Isochrone fitting	J. A. Valenti & D. A. Fischer (2005)
HN Peg	0.1–0.5	0.34 ± 3.34	Chromospheric activity	E. J. Gaidos (1998)
HD 126053[b]	2.3–14.4	13.70 ± 8.53	Chromospheric activity	L. Vican (2012)
GJ 417	0.08–0.3	0.00–5.99	X-ray luminosity	J. D. Kirkpatrick et al. (2000)
HIP 9269[b]	2.2–10.2	17.12 ± 8.68	Isochrone fitting	J. A. Valenti & D. A. Fischer (2005)
G171-58	1.8–3.5	10.30 ± 5.75	Isochrone fitting	J. K. Faherty et al. (2009)
HIP 26653	1.1–9.3	8.12 ± 5.99	Isochrone fitting	J. A. Valenti & D. A. Fischer (2005)
HD 106888	0.3–2.5	0–4.02	Isochrone fitting	Y. G. Shevelev & V. A. Marsakov (1993)
HD 51400	0.6–0.7	3.50 ± 4.63	Color–period diagram	A. Rothermich et al. (2024)
HD 203030	0.13–0.4	1.23 ± 7.08	X-ray emission and chromospheric emission	S. A. Metchev & L. A. Hillenbrand (2006)
HD 8291	$0.89^{+1.30}_{-0.69}$	0–1.46	Gaia photometry	S. Baig et al. (2024)
HD 16270	< 1	4.49 ± 9.08	X-ray emission	J. E. Gizis et al. (2001)
HD 116012[c]	12–14	⋯	Chromospheric activity	J. K. Faherty et al. (2009)
BD +21 55	0.5–10	9.84 ± 33.02	X-ray emission and disklike kinematics	N. R. Deacon et al. (2014)
BD +60 1417[d]	0.01–0.15	0–10.4	Gyrochronology and color–color/period diagrams	J. K. Faherty et al. (2021)
StKM 2-1777[d]	⋯	0–2.61	Chromospheric activity	G. Pace (2013)
HD 253662	< 10	1.63 ± 9.30	Disklike kinematics	N. R. Deacon et al. (2014)
CD –24 407	>1	8.81 ± 9.99	Chromospheric emission	M. Žerjal et al. (2017)
BD +13 2269[d]	⋯	0.39 ± 7.30	⋯	⋯
BD +01 299[d]	6.5–13.5	4.61 ± 14.02	⋯	⋯
StKM 1-1526[d]	⋯	8.18 ± 2.26	⋯	⋯
TYC 5213-545-1[d]	0.1–1	4.63 ± 5.11	Chromospheric emission	M. Žerjal et al. (2017)
LP 617-58[b]	⋯	23.85 ± 5.72	⋯	⋯
HIP 63506[c]	0.3–10	⋯	Disklike kinematics	E. Shkolnik et al. (2009)
LSPM J0632+5053	0.2–10	0–3.33	X-ray flux and disklike kinematics	N. R. Deacon et al. (2014)
NLTT 1011[c]	0.3–10	⋯	Disklike kinematics	N. R. Deacon et al. (2014)
HD 125141	8.5–11	10.25 ± 10.51	Isochrone fitting	J. Holmberg et al. (2009)
BD +06 2986[c]	> 1.6	⋯	Chromospheric activity	D. N. Murray et al. (2011)
BD +24 4329[d]	⋯	9.01 ± 18.72	⋯	⋯
BD +49 2561[d]	⋯	3.23 ± 8.41	⋯	⋯

Notes.
Comparison between previously determined stellar ages and those derived from the [Y/Mg] abundance ratio.
[a] Published age ranges found in the literature.
[b] Implausible old age, as age is older than the estimated age of the Universe, ≈13.8 Gyr.
[c] Only upper limit found for [Y/Mg], so no [Y/Mg] reported age.
[d] Age determined using [Y/Mg]–rotation age relations.

J. Shejeelammal et al. 2024), and FGK stars (T. A. Berger et al. 2022). The [Y/Mg] ratio appears to be correlated with stellar age, reflecting the nucleosynthetic history of the Galactic disk (J. Shejeelammal et al. 2024). Brown dwarfs orbiting solar-type stars provide an excellent opportunity to use the [Y/Mg] chemical clock. Because isolated field brown dwarfs typically have highly uncertain ages, determining the [Y/Mg] ratio of the host star may help to place a spectroscopic age constraint for the entire system.

There are several methods used to estimate the ages of solar analogs. These include gyrochronology, which infers stellar ages from rotation rates of field stars; X-ray emission, where coronal activity serves as an age indicator because magnetic activity decreases as stars spin down over time; and chromospheric emission, arising from the cores of the Ca II H and K lines, which has been observed to decline with stellar age. Lithium abundance is another diagnostic, since lithium is rapidly depleted in the cores of solar-type stars early in their evolution. Additionally, isochrone fitting allows ages to be determined by placing stars on theoretical Hertzsprung–Russell diagrams using observed parameters such as effective temperature ($T_{\rm eff}$), absolute magnitude (M_v), and metallicity ([Fe/H]), along with kinematic information. Some of these methods have previously been applied to different subsets of our sample; here we investigate an abundance-based method that provides another independent check on system age.

T. A. Berger et al. (2022) show that the [Y/Mg] abundance ratio serves as a useful age indicator for FGK-type stars in general but achieves its highest reliability and precision within solar twins and analogs. Here we investigate the age determination for our sample from the [Y/Mg] ratio using the formulation from T. A. Berger et al. (2022) and values for [Y/Mg]–rotation age best-fit relations from the J. M. Brewer & D. A. Fischer (2018) catalog. We present our results in Table 12.

We use the following formulation to determine the age:

$$[\mathrm{Y/Mg}] = m \times \mathrm{age} + b, \quad (8)$$

where for J. M. Brewer & D. A. Fischer (2018) slope (m) = −0.228, intercept (b) = 0.121, and [Y/Mg] are values

Table 13
Estimates of Brown Dwarf Companion Mass from Spectroscopic [Y/Mg] Age Compared to Brown Dwarf Evolutionary Models from the Literature

Companion	L_{Bol}/T_{eff}	M_{Jup} [Y/Mg][a]	M_{Jup} (Literature)	References
HD 89744 B	−3.61 ± 0.03	80.05 ± 10.02	82.92 ± 0.61	UltracoolSheet
HD 46588 B	−4.68 ± 0.05	70.18 ± 14.11	64.0 ± 8.0	UltracoolSheet
2MASS J00250365+4759191	−3.33 ± 0.04	91.18 ± 3.95	84–87	J. K. Faherty et al. (2009)
2MASS J12173646+1427119	−3.64 ± 0.02	55.45 ± 14.25	77.64 ± 8.51	UltracoolSheet
HN Peg B	−4.83 ± 0.05	49.20 ± 11.52	21.00 ± 7.00	G. Suárez et al. (2021)
BD +01 2920B	−4.43 ± 0.15	70.60 ± 7.72,	38.41 ± 24.24	UltracoolSheet
GJ 417BC	−4.12 ± 0.04	70.73 ± 11.97	99 ± 3[b]	T. J. Dupuy et al. (2014)
2MASS J06324849+5053351	−3.71 ± 0.07	75.51 ± 10.25	79.43 ± 11.73	UltracoolSheet
CWISE J065752.45+163350.2[c]	1482 ± 100	67.61 ± 10.08	62.8	A. Rothermich et al. (2024)
HD 8291 B[c]	1625 ± 100	51.43 ± 11.04	$74.6^{+1.3}_{-29.0}$	S. Baig et al. (2024)
2MASS J14165987+5006258	−4.28 ± 0.02	72.27 ± 5.38	74.29 ± 0.27	UltracoolSheet
HD 37216 B	−3.84 ± 0.02	78.17 ± 4.11	80.13 ± 0.95	UltracoolSheet
2MASS J06135342+1514062	−3.26 ± 0.02	92.91 ± 5.92	77.5 ± 31.41	UltracoolSheet
CWISE J132539.70+022309.4[c]	2394 ± 100	…	≈84	A. Rothermich et al. (2024)
HIP 9269B	−4.42 ± 0.03	…	72.25 ± 1.06	UltracoolSheet
HD 3651 B	−5.60 ± 0.06	43.45 ± 7.58	45.96 ± 4.05	UltracoolSheet
HD 202030 B	−4.99 ± 0.10	54.55 ± 15.53	$33.52^{+9.43}_{-12.57}$	S. A. Metchev & L. A. Hillenbrand (2006)
2MASS J13204427+0409045	−3.92 ± 0.03	…	78.07 ± 0.44	UltracoolSheet
WISE J124332.17+600126.6	−4.42 ± 0.10	67.78 ± 11.03	13.47 ± 5.67	C. L. Phillips et al. (2024)
CWISE J214129.80–024623.6[c]	1694 ± 100	72.46 ± 6.74	≈84	A. Rothermich et al. (2024)
2MASS J00302476+2244492	−3.66 ± 0.02	83.69 ± 1.05	81.92 ± 3.91	UltracoolSheet
CWISE J005635.48–240401.9[c]	1336 ± 100	64.93 ± 10.74	52.36	A. Rothermich et al. (2024)
CWISE J165325.10+490439.7[c]	1581 ± 100	69.93 ± 8.39	62.84	A. Rothermich et al. (2024)
ULAS J103131.49+123736.4[c]	1821 ± 100	73.08 ± 8.33	≈84	A. Rothermich et al. (2024)
HD 16270 B	−3.57 ± 0.03	81.65 ± 8.55	82.0 ± 2.67	UltracoolSheet
CWISE J174509.03+380733.2[c]	1694 ± 100	74.64 ± 0.89	62.84	A. Rothermich et al. (2024)
WIS 395 B	−4.31 ± 0.03	52.25 ± 10.37	11.36 ± 0.35	UltracoolSheet
2MASS J13005061+4214473 [c]	2102 ± 100	…	…	J. C. Filippazzo et al. (2015)
CWISE J210640.16+250729.0[c]	1184 ± 100	62.01 ± 9.58	≈ 31.42	A. Rothermich et al. (2024)
2MASS J00193275+4018576	−3.66 ± 0.02	…	81.92 ± 3.91	UltracoolSheet
ULAS J014016.91+015054.7[c]	1149 ± 30	58.78 ± 13.09	…	A. J. Burgasser et al. (2025)
ULAS J150457.65+053800.8[c]	914 ± 100	…	…	A. J. Burgasser et al. (2025)

Notes. Several brown dwarfs have physically implausible old ages (>12 Gyr); as a result, we cannot use evolutionary models to determine a mass.
[a] Mass of companion if [Y/Mg] age is adopted. Mass is not reported if [Y/Mg]-derived age is implausible or if only upper limit for [Y/Mg].
[b] Dynamical mass measurement for the brown dwarf binary GJ 417BC.
[c] T_{eff} determined using the SEDA-based J. C. Filippazzo et al. (2015) spectral type–temperature relationships; an error of 100 K is adopted.

taken from [Y/H]−[Mg/H], and the ratio is presented in Table 8.

To determine the error on the age, we use

$$\sigma_{age} = \text{Age} \times \sqrt{\frac{(\sigma_{[Y/Mg]})^2 + (\sigma_b)^2}{([Y/Mg] - b)^2} + \left(\frac{\sigma_m}{m}\right)^2}, \quad (9)$$

where $\sigma_b = 0.016$ and $\sigma_m = 0.0044$ and $\sigma_{[Y/Mg]}$ is the propagation error of the values of [Y/Mg]. Due to the shallow slope (m), small variations in [Y/Mg] near the intercept (b) sometimes produce negative ages. This occurs primarily for young stars with independent literature constraints (e.g., gyrochronology or isochrones). Because negative ages are unphysical, we truncate the distribution at 0 Gyr. We define their age constraints as an upper physical limit ranging from 0 to (Age + σ_{age}) Gyr.

Our sample has previous literature age estimates from a mix of isochrone fitting, chromospheric activity, X-ray emission, disklike kinematics, which often give wide age estimates (e.g., 0.2−10 Gyr). Generally we find a tighter constraint on ages, but often we find higher estimates on the age from [Y/Mg] than literature estimates. We find that the ages determined from [Y/Mg] for four of our systems (HD 126053, HIP 9269, LP 617-58, *54 Psc) provide implausible ages—ages greater than the age of the Universe (D. N. Spergel et al. 1997). Notably, we find that one target, HD 8291 (G5), provides a [Y/Mg]-derived age in line with previous age estimates; this is the only star with an age estimate from Gaia photometry. In Figure 11 we show the [Y/Mg] versus [Fe/H] determined from Equation (8) for our sample.

6.1. Age Implications for Brown Dwarf Companions

Stellar ages derived from the [Y/Mg] chemical clock can provide a valuable constraint on the evolutionary state of substellar companions and can therefore be used as robust priors when comparing observed brown dwarf luminosities or effective temperatures to evolutionary cooling models. Although age information alone does not uniquely determine brown dwarf masses owing to the inherent age–mass degeneracy, it significantly restricts the range of allowed solutions. We use bolometric luminosity values from the UltracoolSheet[19] in conjunction with our [Y/Mg]-derived ages to place constraints on model-dependent mass values for the brown dwarf companions (A. Burrows et al. 2001; D. Saumon

[19] https://zenodo.org/records/15802304

& M. S. Marley 2008; I. Baraffe et al. 2015, 2002). We use the SPLAT code (A. J. Burgasser & Splat Development Team 2017), where the evolutionary model parameters are derived by loglinear interpolation of the original model grid. When bolometric luminosity measurements are not available in the literature, we use the reported spectral type of the brown dwarf companion to determine the effective temperature using the SEDA code (G. Suarez et al. 2026), which follows the J. C. Filippazzo et al. (2015) spectral type–temperature relationship. For some of our FGK + brown dwarf systems we find that the determined masses from adopting our [Y/Mg]-derived ages are within 1σ–2σ of the literature-reported mass value. These results prove promising in continuing to evaluate the use of the [Y/Mg] age diagnostic for FGK stars and age-dating field brown dwarfs in particular. We provide our findings in Table 13.

7. Conclusions

In this paper, we present a uniform abundance analysis of 32 FGK stars that host benchmark brown dwarfs. We utilize the high-resolution (R = 50,000 and R = 130,000) PEPSI spectrograph on the Large Binocular Telescope to obtain high-SNR (SNR $\geqslant$ 200) data. A fraction of our targets are of particular interest to the brown dwarf and substellar science community, as the companions have current and forthcoming JWST data with NIRSpec/PRISM and MIRI/LRS data (B. Burningham et al. 2023; Z. Zhang et al. 2025a).

We use the BACCHUS framework to determine precise spectroscopic parameters and abundance ratios of our sample, with a focus on elements used to determine the following ratios: C/O, Mg/Si, Ca/Al, S/N, and [Y/Mg]. We summarize the primary conclusions derived from this work:

1. We achieve a typical precision of 42 K in $T_{\rm eff}$ and $\sim$0.03 dex in [Fe/H] for our sample. We have a similar precision of $\sim$0.03 dex for our R = 50,000 and R = 130,000 spectra.
2. In line with previous works, we experience challenges in abundance determination for our coolest K dwarf targets, which often resulted in upper limits for key elements and ratios, like [O/H] and C/O.
3. We use the theoretical chemical frameworks from E. Calamari et al. (2024) to predict cloud species in our brown dwarf companions based on host star Mg/Si ratios. We find that most of our systems predict enstatite and forsterite clouds, with five systems also predicting quartz clouds (Table 9) Future and current retrieval results of the companion with JWST will assist in determining best-fit cloud species to compare to predictions from this work.
4. We compare the C/O of the brown dwarf host star sample with the wide-orbit directly imaged population from A. Baburaj et al. (2025, 2026) and find that our sample exhibits similar chemical diversity for stellar hosts of brown dwarf companions.
5. We use the Si, Mg, Ca, Al, O, and Ti abundances to determine relative oxygen sinks (or sequestering) for our systems (E. Calamari et al. 2024). This has implications for determining the bulk versus retrieved C/O ratio in the brown dwarf companions. We find a median oxygen sink of 21.40% $\pm$ 5.3%, which is higher than the local solar neighborhood value of $17.8^{+1.7}_{-2.3}$%.
6. We continue to test and investigate the use of the [Y/Mg] stellar clock for FGK stars and in particular those that host brown dwarf companions with a wide age estimate (Section 6). We find that for a number of systems our derived ages from [Y/Mg] in combination with fundamental parameters ($L_{\rm Bol}$ or $T_{\rm eff}$) provide mass estimates within 1σ of previous mass estimates (Table 13).

Acknowledgments

This work is dedicated to my late mom, Janet Leigh Phillips (1961−2024). I began this work at the Center for Computational Astrophysics as a CCA Predoc. Less than 3 weeks later, I lost her. My mom was my foundation and the reason I became an astronomer. She saw the first astronomer in me when I was a young child. I hope this work serves as a foundation to help guide my colleagues in grounding and interpreting their analyses of companion brown dwarfs, just as my mom grounded and guided me. Her favorite color was purple, and to honor her, I incorporated purple into all the figures so that she is always with me. I carry my mom's love and care with me in everything I do. "The cosmos is within us. We are made of star-stuff. We are a way for the universe to know itself." My mom has returned to the cosmos, but her love is still here with me. I love and miss you, momma, until we meet again to exchange a hug among the stars.

We thank the anonymous reviewer for the feedback, which improved this paper. C.L.P. thanks Yayaati Chachan for the helpful discussions regarding N/O, C/N, and C/N ratios and their implications with regard to brown dwarfs and Adam Wheeler and Andy Casey for a helpful start to this project. C. L.P. would also like to thank John Brewer for helpful discussions on carbon and oxygen abundances.

C.M. is supported by the NSF Astronomy and Astrophysics Fellowship award No. AST-2401638. J.W. acknowledges the support by the National Science Foundation under grant No. 2143400.

Support for this work was provided by NASA through the NASA Hubble Fellowship grant HST-HF2-51585.001-A awarded by the Space Telescope Science Institute, which is operated by the Association of Universities for Research in Astronomy, Inc., for NASA, under contract NAS5-26555. C.L. P. would like to thank the Center for Computational Astrophysics (CCA) at the Flatiron Institute for their support of this research during her time as a CCA Predoc. The Flatiron Institute is a division of the Simons Foundation. C.L.P. would also like to thank the many people who participated in observational runs and collected data for this project.

E.J.G. acknowledges support for this work provided by NASA through the NASA Hubble Fellowship Program grant No. HST-HF2-51576.001-A awarded by the Space Telescope Science Institute, which is operated by the Association of Universities for Research in Astronomy, Inc., for NASA, under the contract NAS 5-26555.

The research shown here acknowledges use of the Hypatia Catalog, an online compilation of stellar abundance data as described in N. R. Hinkel et al. (2014).

This work is based on observations made with the Large Binocular Telescope. The LBT is an international collaboration

among institutions in the United States, Italy, and Germany. LBT Corporation partners are the University of Arizona on behalf of the Arizona Board of Regents; Istituto Nazionale di Astrofisica, Italy; LBT Beteiligungsgesellschaft, Germany, representing the Max-Planck Society, the Leibniz Institute for Astrophysics Potsdam, and Heidelberg University; The Ohio State University, representing OSU, University of Notre Dame, University of Minnesota, and University of Virginia.

This work presents results from the European Space Agency (ESA) space mission Gaia. Gaia data are being processed by the Gaia Data Processing and Analysis Consortium (DPAC). Funding for the DPAC is provided by national institutions, in particular the institutions participating in the Gaia MultiLateral Agreement (MLA). The Gaia mission website is https://www.cosmos.esa.int/gaia. The Gaia archive website is https://archives.esac.esa.int/gaia.

This work has benefited from The UltracoolSheet at http://bit.ly/UltracoolSheet, maintained by Will Best, Trent Dupuy, Michael Liu, Aniket Sanghi, Rob Siverd, and Zhoujian Zhang and developed from compilations by T. J. Dupuy & M. C. Liu (2012), T. J. Dupuy & A. L. Kraus (2013), N. R. Deacon et al. (2014), M. C. Liu et al. (2016), W. M. J. Best et al. (2018, 2021), A. Sanghi et al. (2023), and A. C. Schneider et al. (2023).

This paper makes use of EXOFAST (J. Eastman et al. 2012) as provided by the NASA Exoplanet Archive, which is operated by the California Institute of Technology, under contract with the National Aeronautics and Space Administration under the Exoplanet Exploration Program.

This research has made use of the SIMBAD database, operated at CDS, Strasbourg, France (M. Wenger et al. 2000).

The land in which this research was finalized is the unceded territory of the Awaswas-speaking Uypi Tribe. The Amah Mutsun Tribal Band, composed of the descendants of indigenous people taken to missions Santa Cruz and San Juan Bautista during Spanish colonization of the Central Coast, is today working hard to restore traditional stewardship practices on these lands and heal from historical trauma.

Facility: Large Binocular Telescope.

Software: `EXOFASTv2` (J. Eastman et al. 2012), `BACCHUS` (T. Masseron et al. 2014), `seda` (G. Suarez et al. 2026), `SPLAT` (A. J. Burgasser & Splat Development Team 2017), numpy (C. R. Harris et al. 2020), astropy (Astropy Collaboration et al. 2013, 2018; Astropy Collaboration et al. 2022).

Appendix A
Solar Fits with BACCHUS

Here we show examples of `BACCHUS` fits for sulfur, nitrogen, oxygen, yttrium, calcium, and carbon for the PEPSI spectra of the Sun from K. G. Strassmeier et al. (2015) in Figure A1.

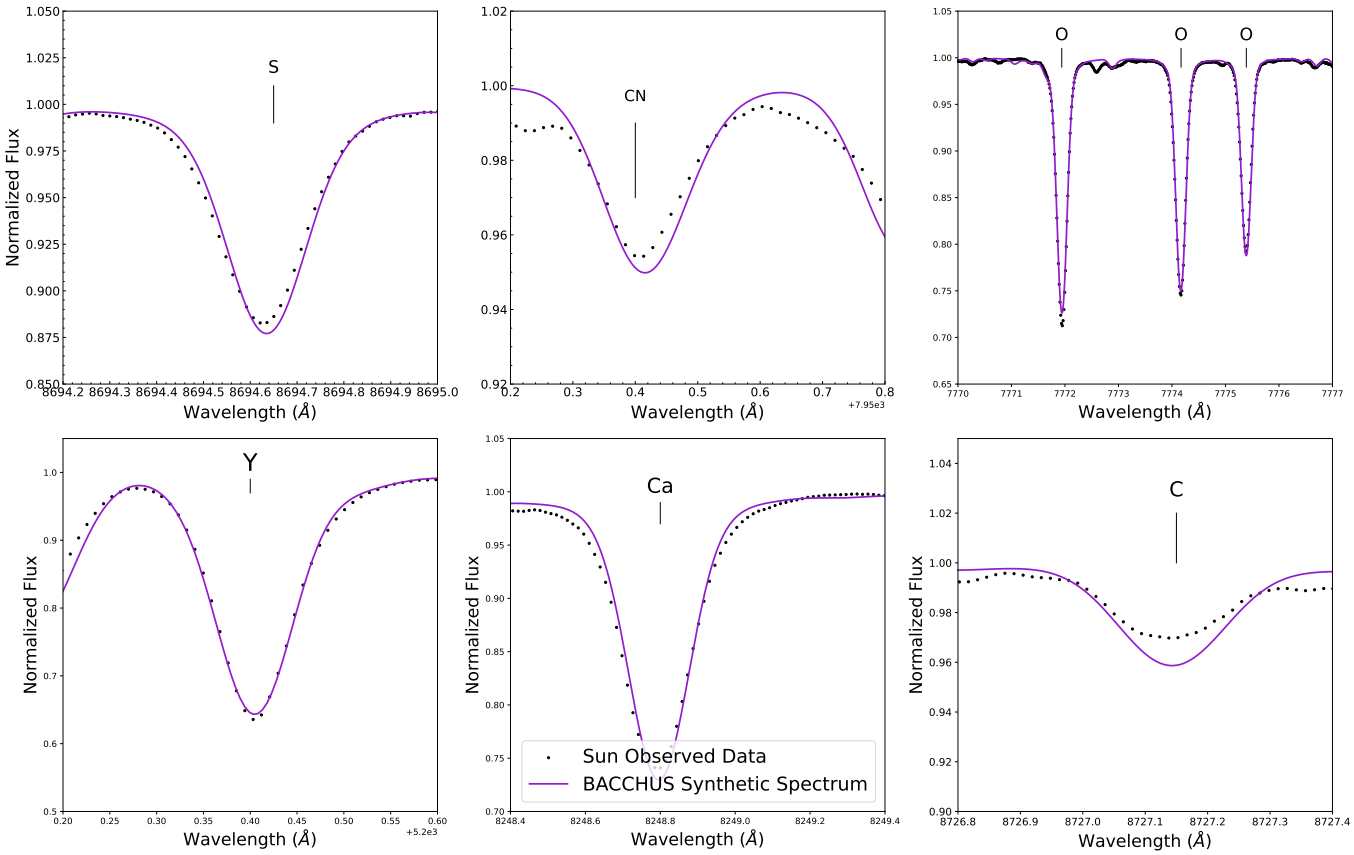


Figure A1. `BACCHUS` fits to the Sun as observed from PEPSI. We show the fits to key features, sulfur, nitrogen, oxygen, yttrium, calcium, and carbon.

Appendix B
Oxygen NLTE Corrections

In Table B1, we provide O I corrections used to calculate the NLTE O I that is used for our C/O calculations.

Table B1
Oxygen Correction Values for the Sample Based on Spectroscopic Stellar Parameters from Table 3

Star	O I [7771.9]	O I [7774.2]	O I [7775.4]
HD 89744	−0.326	−0.301	−0.242
HD 46588	−0.119	−0.102	−0.075
*54 Psc	−0.035	−0.031	−0.024
V* HN Peg	−0.105	−0.092	−0.068
HD 126053	−0.044	−0.037	−0.027
GJ 417	−0.084	−0.073	−0.055
HIP 9269	−0.060	−0.053	−0.040
G171-58	−0.125	−0.111	−0.084
HIP 26653	−0.040	−0.034	−0.026
HD 106888	−0.090	−0.079	−0.059
HD 51400	−0.040	−0.034	−0.026
HD 203030	−0.042	−0.036	−0.027
HD 8291	−0.047	−0.040	−0.030
HD 16270	−0.020	−0.018	−0.014
HD 116012	−0.015	−0.013	−0.010
BD +21 55	−0.014	−0.012	−0.009
BD +60 1417	−0.014	−0.012	−0.009
StKM 2-1777	−0.020	−0.017	−0.013
HD 253662	−0.040	−0.037	−0.029
CD –24 407	−0.021	−0.018	−0.014
BD +13 2269	−0.030	−0.026	−0.020
BD +01 299	−0.011	−0.010	−0.008
StKM 1-1526	−0.032	−0.029	−0.022
TYC 5213-545-1	−0.010	−0.009	−0.007
LP 617-58	−0.019	−0.017	−0.013
LSPM J0632+5053	−0.035	−0.031	−0.024
NLTT 1011	−0.018	−0.016	−0.012
BD +49 2561	−0.013	−0.011	−0.009
HIP 63506	−0.016	−0.014	−0.011
HD 125141	−0.061	−0.052	−0.039
BD +24 4329	−0.014	−0.012	−0.009

ORCID iDs

Caprice L. Phillips https://orcid.org/0000-0001-5610-5328
Megan Bedell https://orcid.org/0000-0001-9907-7742
Catherine Manea https://orcid.org/0000-0002-0900-6076
Alison Duck https://orcid.org/0000-0002-4531-6899
Anusha Pai Asnodkar https://orcid.org/0000-0002-8823-8237
Emily J. Griffith https://orcid.org/0000-0001-9345-9977
Austin Rothermich https://orcid.org/0000-0003-4083-9962
Emily Calamari https://orcid.org/0000-0002-2682-0790
Jacqueline K. Faherty https://orcid.org/0000-0001-6251-0573
Ben Burningham https://orcid.org/0000-0003-4600-5627
Channon Visscher https://orcid.org/0000-0001-6627-6067
Eileen C. Gonzales https://orcid.org/0000-0003-4636-6676
Ilya Ilyin https://orcid.org/0000-0002-0551-046X
Klaus Strassmeier https://orcid.org/0000-0002-6192-6494
Ji Wang https://orcid.org/0000-0002-4361-8885

References

Adams, A. D., Meyer, M. R., Howe, A. R., et al. 2023, AJ, 166, 192
Ahmad, A. A., Commerçon, B., Chabrier, G., & Borderies, A. 2025, ApJL, 991, L32
Allard, F., Hauschildt, P. H., Alexander, D. R., Tamanai, A., & Schweitzer, A. 2001, ApJ, 556, 357
Aller, K. M., Liu, M. C., Magnier, E. A., et al. 2016, ApJ, 821, 120
Alvarez, R., & Plez, B. 1998, A&A, 330, 1109
Arentsen, A., Prugniel, P., Gonneau, A., et al. 2019, A&A, 627, A138
Asplund, M., Grevesse, N., Sauval, A. J., & Scott, P. 2009, ARA&A, 47, 481
Astropy Collaboration, Price-Whelan, A. M., Lim, P. L., et al. 2022, ApJ, 935, 167
Astropy Collaboration, Price-Whelan, A. M., Sipőcz, B. M., et al. 2018, AJ, 156, 123
Astropy Collaboration, Robitaille, T. P., Tollerud, E. J., et al. 2013, A&A, 558, A33
Baburaj, A., Konopacky, Q. M., Theissen, C. A., et al. 2025, AJ, 169, 55
Baburaj, A., Konopacky, Q. M., Theissen, C. A., Gerasimov, R., & Hoch, K. K. W. 2026, AJ, 171, 21
Baghel, P., Goyal, J., & Shukla, G. 2025, MNRAS, 544, 113
Baig, S., Smart, R. L., Jones, H. R. A., et al. 2024, MNRAS, 533, 3784
Baraffe, I., Chabrier, G., Allard, F., & Hauschildt, P. H. 2002, A&A, 382, 563
Baraffe, I., Homeier, D., Allard, F., & Chabrier, G. 2015, A&A, 577, A42
Bate, M. R., Bonnell, I. A., & Bromm, V. 2002, MNRAS, 332, L65
Bedell, M., Meléndez, J., Bean, J. L., et al. 2014, ApJ, 795, 23
Bensby, T., Feltzing, S., & Oey, M. S. 2014, A&A, 562, A71
Bergemann, M., Hoppe, R., Semenova, E., et al. 2021, MNRAS, 508, 2236
Berger, T. A., van Saders, J. L., Huber, D., et al. 2022, ApJ, 936, 100
Best, W. M. J., Liu, M. C., Magnier, E. A., & Dupuy, T. J. 2021, AJ, 161, 42
Best, W. M. J., Magnier, E. A., Liu, M. C., et al. 2018, ApJS, 234, 1
Blanco-Cuaresma, S. 2019, MNRAS, 486, 2075
Boss, A. P. 1997, Sci, 276, 1836
Brandt, G. M., Dupuy, T. J., Li, Y., et al. 2021, AJ, 162, 301
Brewer, J. M., & Fischer, D. A. 2016, ApJ, 831, 20
Brewer, J. M., & Fischer, D. A. 2018, ApJS, 237, 38
Brewer, J. M., Fischer, D. A., Valenti, J. A., & Piskunov, N. 2016, ApJS, 225, 32
Brooke, J. S. A., Bernath, P. F., Schmidt, T. W., & Bacskay, G. B. 2013, JQSRT, 124, 11
Brucalassi, A., Tsantaki, M., Magrini, L., et al. 2022, ExA, 53, 511
Burgasser, A. J., Schneider, A. C., Meisner, A. M., et al. 2025, ApJ, 982, 79
Burgasser, A. J. & Splat Development Team 2017, ASInC, 14, 7
Burningham, B., Faherty, J., Gagné, J., Mann, A., & Hung, C.-L. 2018, RNAAS, 2, 207
Burningham, B., Faherty, J. K., Bardalez Gagliuffi, D. C., et al. 2023, Sinking silicates: tracing rainout across the LT transitionĎ JWST Proposal. Cycle 2, ID. #3670,
Burningham, B., Faherty, J. K., Gonzales, E. C., et al. 2021, MNRAS, 506, 1944
Burrows, A., Heng, K., & Nampaisarn, T. 2011, ApJ, 736, 47
Burrows, A., Hubbard, W. B., Lunine, J. I., & Liebert, J. 2001, RvMP, 73, 719
Cabral, N., Guilbert-Lepoutre, A., Bitsch, B., Lagarde, N., & Diakite, S. 2023, A&A, 673, A117
Calamari, E., Faherty, J. K., Burningham, B., et al. 2022, ApJ, 940, 164
Calamari, E., Faherty, J. K., Visscher, C., et al. 2024, ApJ, 963, 67
Calamari, E., Faherty, J. K., Visscher, C., et al. 2026, ApJL, 1000, L51
Cameron, A. G. W. 1978, M&P, 18, 5
Canty, J. I., Lucas, P. W., Roche, P. F., & Pinfield, D. J. 2013, MNRAS, 435, 2650
Casagrande, L., Schönrich, R., Asplund, M., et al. 2011, A&A, 530, A138
Casali, G., Magrini, L., Tognelli, E., et al. 2019, A&A, 629, A62
Chabrier, G., & Baraffe, I. 1997, A&A, 327, 1039
Chiu, K., Fan, X., Leggett, S. K., et al. 2006, AJ, 131, 2722
Costes, J. C., Xuan, J. W., Vigan, A., et al. 2024, A&A, 686, A294
Crepp, J. R., Gonzales, E. J., Bechter, E. B., et al. 2016, ApJ, 831, 136
Cutri, R. M., Skrutskie, M. F., van Dyk, S., et al. 2003, yCat, 2246, 0
da Silva, R., Danielski, C., Delgado Mena, E., et al. 2024, A&A, 688, A193
Deacon, N. R., Liu, M. C., Magnier, E. A., et al. 2014, ApJ, 792, 119
Delgado Mena, E., Israelian, G., González Hernández, J. I., et al. 2010, ApJ, 725, 2349
Dotter, A. 2016, ApJS, 222, 8

Dupuy, T. J., & Kraus, A. L. 2013, Sci, 341, 1492
Dupuy, T. J., & Liu, M. C. 2012, ApJS, 201, 19
Dupuy, T. J., Liu, M. C., & Ireland, M. J. 2014, ApJ, 790, 133
Eastman, J., Gaudi, B. S., & Agol, E. 2012, EXOFAST: Fast transit and/or RV fitter for single exoplanet, Astrophysics Source Code Library, ascl: 1207.001
Eastman, J. D., Rodriguez, J. E., Agol, E., et al. 2019, arXiv:1907.09480
Faherty, J. K., Burgasser, A. J., West, A. A., et al. 2009, AJ, 139, 176
Faherty, J. K., Gagné, J., Popinchalk, M., et al. 2021, ApJ, 923, 48
Faherty, J. K., Riedel, A. R., Cruz, K. L., et al. 2016, ApJS, 225, 10
Feng, F., Butler, R. P., Vogt, S. S., et al. 2022, ApJS, 262, 21
Filippazzo, J. C., Rice, E. L., Faherty, J., et al. 2015, ApJ, 810, 158
Fischer, D. A., & Valenti, J. 2005, ApJ, 622, 1102
Fontanive, C., Bedin, L. R., De Furio, M., et al. 2023, MNRAS, 526, 1783
Franson, K., & Bowler, B. P. 2023, AJ, 165, 246
Franson, K., Bowler, B. P., Brandt, T. D., et al. 2022, AJ, 163, 50
Gaarn, J., Burningham, B., Faherty, J. K., et al. 2023, MNRAS, 521, 5761
Gagné, J. 2024, PASP, 136, 063001
Gagné, J., Moranta, L., Faherty, J. K., et al. 2023, ApJ, 945, 119
Gaia Collaboration, Vallenari, A., Brown, A. G. A., et al. 2023, A&A, 674, A1
Gaidos, E. J. 1998, PASP, 110, 1259
García Pérez, A. E., Sánchez-Blázquez, P., Vazdekis, A., et al. 2021, MNRAS, 505, 4496
Gizis, J. E., Kirkpatrick, J. D., & Wilson, J. C. 2001, AJ, 121, 2185
Gomes, J. I., Pinfield, D. J., Marocco, F., et al. 2013, MNRAS, 431, 2745
Grevesse, N., Asplund, M., & Sauval, A. J. 2007, SSRv, 130, 105
Grieves, N., Ge, J., Thomas, N., et al. 2017, MNRAS, 467, 4264
Gustafsson, B., Edvardsson, B., Eriksson, K., et al. 2008, A&A, 486, 951
Hackshaw, Z., Hawkins, K., & Manea, C. 2025, ApJ, 995, 140
Harris, C. R., Millman, K. J., van der Walt, S. J., et al. 2020, Natur, 585, 357
Hawkins, K., Lucey, M., Ting, Y.-S., et al. 2020, MNRAS, 492, 1164
Hayes, C. R., Masseron, T., Sobeck, J., et al. 2022, ApJS, 262, 34
Heiter, U., Lind, K., Bergemann, M., et al. 2021, A&A, 645, A106
Hejazi, N., Crossfield, I. J. M., Souto, D., et al. 2024, ApJ, 973, 31
Helling, C., Woitke, P., & Thi, W. F. 2008, A&A, 485, 547
Hinkel, N. R., Timmes, F. X., Young, P. A., Pagano, M. D., & Turnbull, M. C. 2014, AJ, 148, 54
Hinkel, N. R., Young, P. A., Pagano, M. D., et al. 2016, ApJS, 226, 4
Hinkel, N. R., Young, P. A., & Wheeler, C. H., III 2022, AJ, 164, 256
Hoch, K. K. W., Konopacky, Q. M., Theissen, C. A., et al. 2023, AJ, 166, 85
Hoch, K. K. W., Rowland, M., Petrus, S., et al. 2025, Natur, 643, 938
Holland, W. S., Matthews, B. C., Kennedy, G. M., et al. 2017, MNRAS, 470, 3606
Holmberg, J., Nordström, B., & Andersen, J. 2009, A&A, 501, 941
Hsu, C.-C., Wang, J. J., Xuan, J. W., et al. 2024, ApJ, 971, 9
Huber, D., Chaplin, W. J., Christensen-Dalsgaard, J., et al. 2013, ApJ, 767, 127
Jofré, P., Heiter, U., & Soubiran, C. 2019, ARA&A, 57, 571
Kammerer, J., Winterhalder, T. O., Lacour, S., et al. 2025, A&A, 704, A318
Katime Santrich, O. J., Kerber, L., Abuchaim, Y., & Gonçalves, G. 2022, MNRAS, 514, 4816
Kiefer, F., Hébrard, G., Sahlmann, J., et al. 2019, A&A, 631, A125
Kirkpatrick, J. D. 2005, ARA&A, 43, 195
Kirkpatrick, J. D., Cruz, K. L., Barman, T. S., et al. 2008, ApJ, 689, 1295
Kirkpatrick, J. D., Reid, I. N., Liebert, J., et al. 2000, AJ, 120, 447
Kolecki, J. R., & Wang, J. 2022, AJ, 164, 87
Kramida, A., Ralchenko, Y., Reader, J. & NIST ASD Team 2023, NIST Atomic Spectra Database (ver. 5.11),
Landman, R., Stolker, T., Snellen, I. A. G., et al. 2024, A&A, 682, A48
Lee, J., & Song, I. 2024, ApJ, 967, 113
Lewis, J. S. 2004, International Geophysics, Physics and Chemistry of the Solar System (Elsevier), 77
Liu, M. C., Dupuy, T. J., & Allers, K. N. 2016, AJ, 833, 96
Lodders, K. 2002, ApJ, 577, 974
Lodders, K. 2003, ApJ, 591, 1220
Loutrel, N. P., Luhman, K. L., Lowrance, P. J., & Bochanski, J. J. 2011, ApJ, 739, 81
Luck, R. E. 2017, AJ, 153, 21
Luck, R. E. 2018, AJ, 155, 111
Ma, B., & Ge, J. 2014, MNRAS, 439, 2781
Mack, C. E., Strassmeier, K. G., Ilyin, I., et al. 2018, A&A, 612, A46
Maire, A.-L., Leclerc, A., Balmer, W. O., et al. 2024, A&A, 691, A263
Maldonado, J., & Villaver, E. 2017, A&A, 602, A38
Marley, M. S., Seager, S., Saumon, D., et al. 2002, ApJ, 568, 335
Marocco, F., Pinfield, D. J., Cook, N. J., et al. 2017, MNRAS, 470, 4885
Masseron, T., Plez, B., Van Eck, S., et al. 2014, A&A, 571, A47
Mata Sánchez, D., González Hernández, J. I., Israelian, G., et al. 2014, A&A, 566, A83
Metchev, S. A., & Hillenbrand, L. A. 2006, ApJ, 651, 1166
Meynardie, W. W., Meyer, M. R., MacDonald, R. J., et al. 2025, ApJ, 994, 237
Moore, C. E., Minnaert, M. G. J., & Houtgast, J. 1966, National Bureau of Standards Monograph, The Solar Spectrum 2935 A to 8770 A (USGPO)
Morley, C. V., Fortney, J. J., Marley, M. S., et al. 2012, ApJ, 756, 172
Morris, B. M., Curtis, J. L., Sakari, C., Hawley, S. L., & Agol, E. 2019, AJ, 158, 101
Mortier, A., Sousa, S. G., Adibekyan, V. Z., Brandão, I. M., & Santos, N. C. 2014, A&A, 572, A95
Murray, D. N., Burningham, B., Jones, H. R. A., et al. 2011, MNRAS, 414, 575
Neves, V., Santos, N. C., Sousa, S. G., Correia, A. C. M., & Israelian, G. 2009, A&A, 497, 563
Nissen, P. E. 2015, A&A, 579, A52
Öberg, K. I., Facchini, S., & Anderson, D. E. 2023, ARA&A, 61, 287
Öberg, K. I., Murray-Clay, R., & Bergin, E. A. 2011, ApJL, 743, L16
Ortega, V. G., Jilinski, E., De La Reza, R., & Bazzanella, B. 2007, MNRAS, 377, 441
Pace, G. 2013, A&A, 551, L8
Perri, A. N., & McKemmish, L. K. 2024, MNRAS, 531, 3023
Phillips, C. L., Bowler, B. P., Mace, G., Liu, M. C., & Sokal, K. 2020, ApJ, 896, 173
Phillips, C. L., Faherty, J. K., Burningham, B., et al. 2024, ApJ, 972, 172
Phillips, M. W., Liu, M. C., & Zhang, Z. 2024, ApJ, 961, 210
Pietrow, A. G. M., Baratella, M., Ilyin, I. V., Steffen, M., & Strassmeier, K. G. 2026, A&A, 706, L11
Pinfield, D. J., Burningham, B., Lodieu, N., et al. 2012, MNRAS, 422, 1922
Plez, B. 2012, Turbospectrum: Code for spectral synthesis, Astrophysics Source Code Library, ascl: 1205.004
Polanski, A. S., Crossfield, I. J. M., Howard, A. W., Isaacson, H., & Rice, M. 2022, RNAAS, 6, 155
Prugniel, P., Vauglin, I., & Koleva, M. 2011, A&A, 531, A165
Ralchenko, Y., & Kramida, A. 2020, Atoms, 8, 56
Ratcliffe, B., Minchev, I., Cescutti, G., et al. 2024, MNRAS, 528, 3464
Reggiani, H., Galarza, J. Y., Schlaufman, K. C., et al. 2024, AJ, 167, 45
Reid, I. N., Lewitus, E., Allen, P. R., Cruz, K. L., & Burgasser, A. J. 2006, AJ, 132, 891
Rice, M., & Brewer, J. M. 2020, ApJ, 898, 119
Rickman, E. L., Ceva, W., Matthews, E. C., et al. 2024, A&A, 684, A88
Rothermich, A., Faherty, J. K., Bardalez-Gagliuffi, D., et al. 2024, AJ, 167, 253
Rothermich, A., Faherty, J. K., Burningham, B., et al. 2026, ApJ, submitted
Ryabchikova, T., Piskunov, N., & Pakhomov, Y. 2022, Atoms, 10, 103
Ryabchikova, T., Piskunov, N., Pakhomov, Y., et al. 2015, MNRAS, 456, 1221
Sahlmann, J., Ségransan, D., Queloz, D., et al. 2011, A&A, 525, A95
Sanchez, J. A., Smith, P. C. B., Kanumalla, K., et al. 2026, NatCo, 17, 2902
Sanghi, A., Liu, M. C., Best, W. M. J., et al. 2023, ApJ, 959, 63
Saumon, D., & Marley, M. S. 2008, ApJ, 689, 1327
Schneider, A. C., Cushing, M. C., Kirkpatrick, J. D., et al. 2014, AJ, 147, 34
Schneider, A. C., Munn, J. A., Vrba, F. J., et al. 2023, AJ, 166, 103
Shejeelammal, J., Meléndez, J., Rathsam, A., & Martos, G. 2024, A&A, 690, A107
Shevelev, Y. G., & Marsakov, V. A. 1993, AZh, 70, 1218
Shkolnik, E., Liu, M. C., & Reid, I. N. 2009, ApJ, 699, 649
Sinha, A., Zasowski, G., Myers, N. R., et al. 2026, MNRAS, 547, stag440
Sitnova, T. M., Mashonkina, L. I., & Ryabchikova, T. A. 2013, AstL, 39, 126
Skrzypek, N., Warren, S. J., & Faherty, J. K. 2016, A&A, 589, A49
Socas-Navarro, H. 2015, A&A, 577, A25
Spergel, D. N., Bolte, M., & Freedman, W. 1997, PNAS, 94, 6579
Stonkutė, E., Chorniy, Y., Tautvaišienė, G., et al. 2020, AJ, 159, 90
Strassmeier, K. G., Ilyin, I., Järvinen, A., et al. 2015, AN, 336, 324
Strassmeier, K. G., Ilyin, I., & Steffen, M. 2018a, A&A, 612, A44
Strassmeier, K. G., Ilyin, I., Weber, M., et al. 2018b, SPIE, 10702, 1070212
Suárez, G., Cruz, K., Faherty, J. K., et al. 2026, JOSS, submitted
Suárez, G., Metchev, S., Leggett, S. K., Saumon, D., & Marley, M. S. 2021, ApJ, 920, 99
Sun, Q., Ji, C., Wang, S. X., et al. 2025, A&A, 701, A107
Tautvaišienė, G., Drazdauskas, A., Mikolaitis, Š., et al. 2015, A&A, 573, A55
Teixeira, J., Adibekyan, V., & Bossini, D. 2025, AN, 346, e20240076
Teske, J. K. 2024, ARA&A, 62, 333
Torres, G., Andersen, J., & Giménez, A. 2010, A&ARv, 18, 67
Tsantaki, M., Sousa, S. G., Adibekyan, V. Z., et al. 2013, A&A, 555, A150
Tucci Maia, M., Ramírez, I., Meléndez, J., et al. 2016, A&A, 590, A32

Turrini, D., Schisano, E., Fonte, S., et al. 2021, ApJ, 909, 40
Valenti, J. A., & Fischer, D. A. 2005, ApJS, 159, 141
Valenti, J. A., & Piskunov, N. 1996, A&AS, 118, 595
Vican, L. 2012, AJ, 143, 135
Visscher, C., Lodders, K., & Fegley, B., Jr. 2006, ApJ, 648, 1181
Vowell, N., Dong, J., Rodriguez, J. E., et al. 2025, MNRAS, 545, staf2161
Wakeford, H. R., Visscher, C., Lewis, N. K., et al. 2016, MNRAS, 464, 4247
Wang, J., Kolecki, J. R., Ruffio, J.-B., et al. 2022, AJ, 163, 189
Wang, R., Luo, A.-L., Chen, J.-J., et al. 2020, ApJ, 891, 23
Wenger, M., Ochsenbein, F., Egret, D., et al. 2000, A&AS, 143, 9
Wilson, J. C., Kirkpatrick, J. D., Gizis, J. E., et al. 2001, AJ, 122, 1989
Woitke, P., Helling, C., & Gunn, O. 2020, A&A, 634, A23
Wright, E. L., Eisenhardt, P. R. M., Mainzer, A. K., et al. 2010, AJ, 140, 1868
Xiang, M., Ting, Y.-S., Rix, H.-W., et al. 2019, ApJS, 245, 34
Xuan, J. W., Hsu, C.-C., Finnerty, L., et al. 2024a, ApJ, 970, 71
Xuan, J. W., Mérand, A., Thompson, W., et al. 2024b, Natur, 634, 1070
Xuan, J. W., Wang, J., Ruffio, J.-B., et al. 2022, ApJ, 937, 54
Žerjal, M., Zwitter, T., Matijevič, G., et al. 2017, ApJ, 835, 61
Zhang, M., Xiang, M., Ting, Y.-S., et al. 2024, ApJS, 273, 19
Zhang, Z., Fortney, J., Molliere, P., et al. 2025a, Empirically anchoring the physics of silicate clouds using L0- T9 benchmark brown dwarfs, JWST Proposal. Cycle 4, ID. #8140,
Zhang, Z., Mollière, P., Fortney, J. J., & Marley, M. S. 2025b, AJ, 170, 64
Zhang, Z., Mollière, P., Hawkins, K., et al. 2023, AJ, 166, 198
Zhang, Z. H., Burgasser, A. J., Gálvez-Ortiz, M. C., et al. 2019, MNRAS, 486, 1260
Zhang, Z. H., Navarete, F., Gálvez-Ortiz, M. C., et al. 2025, MNRAS, 542, 656
Zong, W., Fu, J.-N., De Cat, P., et al. 2020, ApJS, 251, 15